ACOUSTIC DETECTION OF ULTRA-HIGH ENERGY NEUTRINOS

A DISSERTATION
SUBMITTED TO THE DEPARTMENT OF APPLIED PHYSICS
AND THE COMMITTEE ON GRADUATE STUDIES
OF STANFORD UNIVERSITY
IN PARTIAL FULFILLMENT OF THE REQUIREMENTS
FOR THE DEGREE OF
DOCTOR OF PHILOSOPHY

Naoko Kurahashi
August 2010

This dissertation is online at: http://purl.stanford.edu/qn216rx5962

I certify that I have read this dissertation and that, in my opinion, it is fully adequate in scope and quality as a dissertation for the degree of Doctor of Philosophy.

Giorgio Gratta, Primary Adviser

I certify that I have read this dissertation and that, in my opinion, it is fully adequate in scope and quality as a dissertation for the degree of Doctor of Philosophy.

Vahe Petrosian, Co-Adviser

I certify that I have read this dissertation and that, in my opinion, it is fully adequate in scope and quality as a dissertation for the degree of Doctor of Philosophy.

Patricia Burchat

Approved for the Stanford University Committee on Graduate Studies.

Patricia J. Gumport, Vice Provost Graduate Education

This signature page was generated electronically upon submission of this dissertation in electronic format. An original signed hard copy of the signature page is on file in University Archives.

Abstract

Understanding the origin and evolution of cosmic accelerators by measuring ultra-high energy (UHE, $E > 10^{18}$ eV) cosmic rays is one of the main goals of astroparticle physics. UHE neutrinos are thought to be better indicators of cosmic accelerators since they travel from their source undeflected by magnetic fields and unimpeded by interactions with the cosmic microwave background. Both cosmic rays and neutrinos have extremely low fluxes ($< 1 km^{-2} yr^{-1}$) at these energies, which makes measurements difficult. Neutrino measurements have the added challenge of a longer interaction length that makes the atmosphere not suitable as a target. Here, we present the Study of Acoustic Ultra-high energy Neutrino Detection (SAUND) which uses an underwater acoustic sensor array spanning $\sim$1500 km^3 to search for UHE neutrinos interacting in the ocean.

A description of the data acquisition system, results of the background noise study, and an analysis based on an integrated 130 days of data are presented here. Two events are found to have properties compatible with UHE-neutrino-induced particle showers in the energy ranges 10^{24} eV$<E_{sh}<5\times10^{24}$ eV and 10^{22} eV$<E_{sh}<5\times10^{22}$ eV. Since our understanding of transient backgrounds is limited, a flux upper limit is set providing the most sensitive limit to date on UHE neutrinos using the acoustic technique.

Acknowledgments

This work was supported, in part, by the National Science Foundation under grant PHY-0457273. Data acquisition was in courtesy of the US Navy's Naval Undersea Warfare Center (NUWC) and specifically, the Atlantic Undersea Test and Evaluation Center (AUTEC). I'd like to thank everyone at AUTEC that made my trips there enjoyable. The beautiful Andros Island of The Bahamas with its interesting coastlines, blue holes, creeks, mangroves, reefs and beaches was a pleasure to visit and also to gaze down upon from the small AUTEC plane every time I flew in and out. Andros conch fritters are the best.

For sharing her acoustic and "Navy" expertise, I would like to thank Daphne Kapolka of the Naval Postgraduate School. Many former research group members have helped me and this "collaboration-less" experiment, namely, Jason Detwiler who taught me C++ and vi (best text editor), Sam Waldman who shared many LIGO analysis techniques with me, Nikolai Lehtinen whose calculations and codes I still use, and Justin Vandenbroucke who guided me throughout this project. Many thanks to Peter Graham for being my go-to theorist and patiently explaining models and calculations to me. My friends at KIPAC have answered 7 years worth of astronomy questions that ranged from basic to exotic and still remain good friends with me.

I would like to thank my advisor Giorgio Gratta, from whom I have learned so much about neutrinos, physics, and research in general. Nikolai and Kazumi Tolich, Peter Fierlinger, Francisco LePort, Kevin O'sullivan, Maria Montero Diaz, Karl Twelker, Andrea Pocar, Jesse Wodin and the rest of the Gratta research group members that I was fortunate enough to overlap with made my work days at Stanford so enjoyable. Many people in the KamLAND and EXO collaborations have become

good friends and mentors to me, and I thank them for their friendship, guidance and advice. In particular, I'd like to thank Sanshiro Enomoto for believing in my abilities as a physicist before anyone else including myself. Without his mentorship, I would not be where I am today. A big thanks to Matthew Green for his friendship and camaraderie throughout the years. Russell Neilson supported me patiently and enthusiastically through the best of times and the worst of times, through the age of wisdom and the age of foolishness, during the epoch of belief and the epoch of incredulity, through the season of Light and the season of Darkness, through the spring of hope and the winter of despair for good or for evil [1].

Finally, I would like to thank my brother Takafumi who is the smarter one of us two, and my parents Ayako and Kiyotaka Kurahashi for always being understanding, and giving me the freedom and support to pursue whatever path I chose.

Contents

List of Tables

List of Figures

Chapter 1

Introduction

Discovering and understanding the unique properties of neutrinos has long been, and remains, the aim of many particle physics experiments. In the late 1960's, the Homestake experiment found a deficit in the solar electron-neutrino flux compared to the "Standard Solar Model" and thus made the first observation of neutrino oscillation [2]. Thus the sun became the first astronomical object observed via neutrinos. Neutrinos detected by Kamiokande II [3], IMB [4] and Baksan Neutrino Observatory [5] made supernova 1987A the next astronomical source to be observed. To this day, these remain the only two confirmed astronomical neutrino sources. However, neutrinos are thought to be emitted not only by stars and supernovae, but many other astronomical objects and cosmological events. Efforts to measure these neutrinos, which are expected to span a large energy range, are underway. Study of Acoustic Ultra-high Energy Neutrino Detection (SAUND) is a novel experiment that attempts to measure the highest energy neutrinos.

1.1 Neutrinos in Astrophysics

1.1.1 Astronomy and Cosmology

Neutrinos play a key role at the intersection of particle physics and astronomy. Implementing neutrinos and their unique characteristics is now crucial in modeling supernova explosions, pulsars, and many other astrophysical and cosmological events. For example, in the "Standard Cosmological Model," also known as the Lambda CDM model, most of the matter in our universe is in the form of dark matter. While the particle(s) of dark matter are still unknown, the neutrino mass limit from tritium decay [6] of $M_\nu < 2$ eV can be used to determine that neutrinos make up an upper limit of 4% of the matter-energy budget of the universe [7] as "hot dark matter." Conversely, observational cosmology now offers limits on the number of neutrino species and neutrino masses. The most recent analysis [8] suggests that in a spatially flat cosmological constant model, the effective number of neutrino species $N_{eff} = 3.7 \pm 0.7$ and the species-summed neutrino mass $M_\nu < 0.70$ eV at the 95.4 percent confidence level. It is interesting to note that the limit on neutrino mass is better than any limit set by particle physics experiments.

1.1.2 Cherenkov Neutrino Telescopes

Another highlight of neutrinos in astrophysics is the set of major neutrino telescope experiments such as IceCube [9], ANTARES [10], NEMO [11], and Baikal [12]. All of these experiments detect Cherenkov light that originates in the particle showers induced by neutrinos. Optical detectors are deployed in transparent media which also act as targets for neutrinos in the TeV to PeV range. Neutrinos of lower energy cannot be detected due to their short radiation length of Cherenkov light compared to detector spacings. At higher energies, the flux is too low for the volume of these detectors to be sufficient. Cherenkov neutrino-telescope experiments use well established particle-physics detection techniques yet one of their primary goals is to make astronomical observations by locating point sources in the sky.

1.2 The Ultra-high Energy Regime of Cosmic Rays

Modern cosmic-ray physics experiments detecting charged particles offer clues about astronomical sources complementary to optical, x-ray, and other electromagnetic radiation telescopes. They also provide particle physics a natural laboratory with a wide range of accessible energies as shown in Fig. 1.1. Of these extensive energy scales, the so called ultra-high energy (UHE) regime, usually indicating beyond 10^{18} eV or EeV, has received significant attention. Observatories such as the Pierre Auger Observatory [13] cover an expansive area to probe the Greisen-Zatsepin-Kuzmin (GZK) mechanism [14, 15] in this regime. Cosmic rays at these energies are thought to be protons or heavier nuclei. The GZK mechanism argues that because the microwave background becomes opaque to these particles at UHE, a cutoff in the cosmic ray spectrum should be observed. An important consequence of this mechanism is UHE neutrino production from the decays of pions created by the neutrino-microwave photon interaction. Unlike other particles, neutrinos can propagate without interacting with the microwave background or being affected by magnetic fields, thus retaining their energy and direction. This argument also applies to neutrinos produced directly at energetic astronomical sources, such as gamma ray bursts, active galactic nuclei, Z-bursts and other exotic processes. Therefore, neutrinos are predicted to be an important composition in UHE astronomy.

1.3 UHE Neutrino Detectors

Neutrino flux in the UHE regime is expected to be extremely small as hinted at by the cosmic ray flux in that regime. Therefore, an experiment aimed at detecting these neutrinos requires a large target volume. As mentioned before, optical neutrino telescopes have a limit to how large the target can be made, not because of the lack of target material, which are all "nature made" targets such as the ocean, but because the sensor spacing required by the optical depth of the signal makes the number of sensors required in such a large volume impractical. Alternative detectable signals

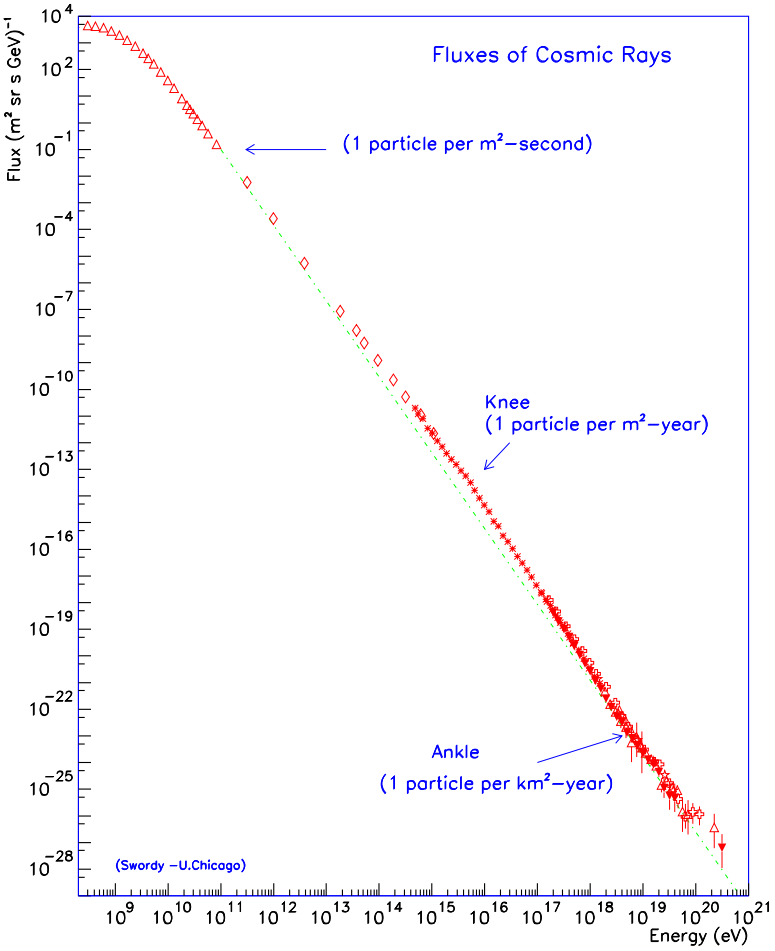

Figure 1.1: The cosmic ray spectrum roughly follows a power law of $E^{-2.5}$ to E^{-3} over many decades of energy [16]. A cutoff to this power law is expected in the UHE regime.

with longer attenuation lengths that originate in UHE neutrino interactions are sound and radio waves.

1.3.1 Acoustic Detectors

Sound waves are produced from the expansion of detector media caused by energy deposition from neutrino-induced showers. Particles produced in the shower eventually pass on their energy as heat to its media. Theoretical models [17, 18] and

experimental measurements [19] show that the acoustic signature of showers is a single bipolar pulse, with acoustic energy concentrated around 10 kHz. The experiment discussed in this thesis as well as the ACoRNE experiment [20] use acoustic sensor arrays deployed for naval warfare purposes to look for UHE neutrino signals. Other experiments such as SPATS [21], ONDE [22], AMADEUS [23], and Baikal [24] deploy their own dedicated acoustic sensors along with their host optical Cherenkov neutrino telescopes, IceCube, NEMO, ANTARES and Baikal, respectively. The main advantage of the array used for the work in this thesis is its extensive area of coverage by an existing working array. The cost of deploying and maintaining such a large array is not feasible for small collaborations pursuing acoustic UHE neutrino detection. On the other hand, collaborations deploying their own sensors may have fewer sensors, but they are able to configure their array optimally for neutrino detection.

1.3.2 Radio and Other Detectors

Radio Cherenkov emission occurring in showers has been shown in laboratories to be coherent and detectable [25]. Experiments such as FORTE [26], RICE [27], and ANITA [28] look for radio emission from the ice layers in Greenland and Antarctica, while GLUE [29], LUNASKA [30], and NuMoon [31] look for radio signals originating from the moon. Radio antennas are also planned to be installed in IceCube and Auger. SalSA [32] is developing a detector using salt domes to look for radio signals as well as possibly acoustic signals originating in UHE neutrino showers. The Auger Observatory is not optimized for UHE neutrino detection due to its target (atmosphere) and the signal they are sensitive to with their surface detectors (Cherenkov light in the optical). However, tau leptons from ν_τ interactions with the earth can emerge and decay causing nearly horizontal showers. By examining inclined showers in the vast area covered by the surface detectors, the Auger collaboration have set a tau neutrino flux limit in this regime [33].

1.4 An Investigative Tool for Relic Neutrinos

One of the most exciting future possibilities of a successful, high sensitivity UHE neutrino telescope is the detection of relic neutrino signatures in the UHE neutrino spectrum. Because UHE neutrinos and relic neutrinos interact at the Z-boson mass to pair produce, a dip in the UHE neutrino spectrum is expected. The challenge to this relic neutrino probe, if enough UHE neutrino flux is present to perform such a measurement, is the redshifting of UHE neutrinos and the various non-zero relic neutrino energies at different astronomical distances along the interaction length [34]. Both of these phenomena result in a washing out of the dip feature in the spectrum as shown in Fig. 1.2. The detection of relic neutrino signatures, however, remains an exciting prospect.

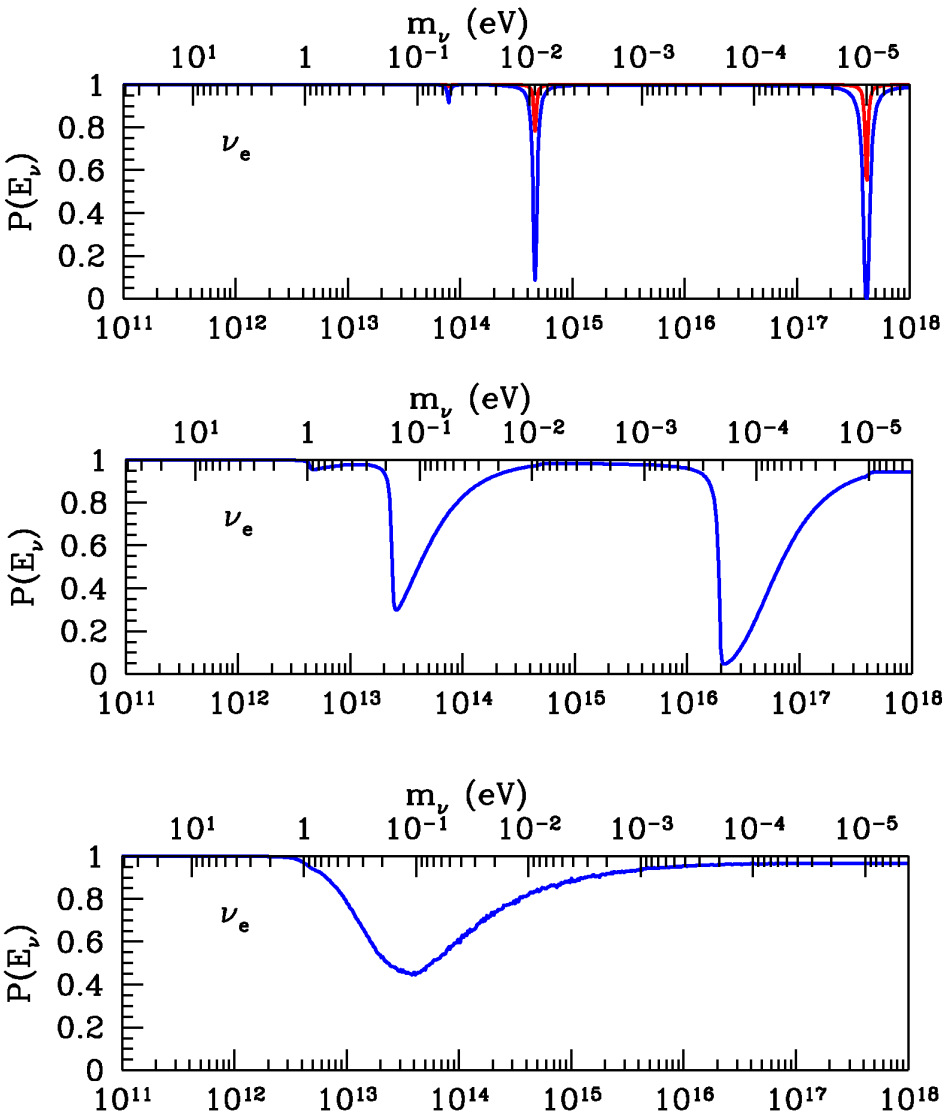

Figure 1.2: Survival probabilities for UHE neutrinos at different energies due to relic neutrino interactions at the Z-boson mass. A normal hierarchy with lowest neutrino mass $m_1 = 10^{-5}$ eV is assumed. The top panel shows the survival probabilities for an UHE neutrino originating 10^4 Mpc (red) and 10^5 Mpc (blue) away. The middle panel includes effects of redshift integrated from z = 20. Bottom panel further includes effects of Fermi smearing due to thermal motion of the relic neutrinos [34].

Chapter 2

Expected Signal

2.1 Choosing A Target Material

As mentioned before, because the UHE neutrino flux is predicted to be very small, detectors must have a very large target volume. The target must be of a naturally existing material at volumes beyond what is constructable. Fig. 2.1 shows the interaction length of UHE neutrinos in different media. Neutrino-nucleon cross sections have not been measured at UHEs. For Fig. 2.1 and throughout this thesis, the cross sections are taken from Gandhi et al [35]. Since our atmosphere is only $\sim 10^6$ cm thick, it remains mostly transparent to neutrinos even at UHEs, and a denser target is needed. Solid earth, ice, and liquid water serve as better detector targets due to their higher nucleon densities. Furthermore, for detectors on earth, the atmosphere serves as a shield for any other UHE particles.

Table 2.1 compares parameters relevant for acoustic coupling in different target materials taken from [36]. T is the temperature of the material considered, $\langle v \rangle$ is the average speed of sound, β is the coefficient of thermal expansion, and C_p is the specific heat. The Gruneisen constant scales with the neutrino-induced pressure signal strength in each material. Although the Gruneisen parameter indicates better coupling with ice and salt, salt domes with large volumes of low impurities are difficult to find as indicated by the "maximum practical volume." While ice remains an interesting medium, recent measurements [37] reveal that attenuation is considerably

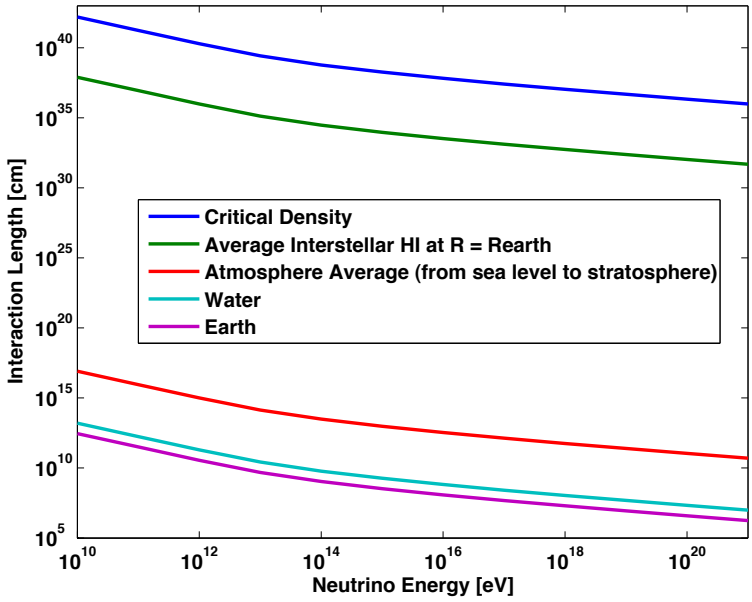

Figure 2.1: Interaction length of UHE neutrinos at different energies in different media: the critical density of the universe, the average desnity of interstellar neutral hydrogen at the radius R = R_{earth} measured from the galactic origin, earth's atmosphere, water, and solid earth.

larger than previous theoretical estimates. The main advantage to using the ocean is the large volume accessible. In this thesis, 1500 km^3 of the ocean is used as a target for an UHE neutrino detector.

2.2 Acoustic Signature in Sea Water

2.2.1 Energy-Signal Coupling

Detector targets must also have good energy-signal coupling. For acoustic signals, the wave equation is used to determine the pressure pulse produced by a given energy deposition:

$$\nabla^2(p + \frac{1}{\omega_0}\dot{p}) - \frac{1}{c^2}\ddot{p} = -\frac{\beta}{C_p}\frac{\partial E}{\partial t}. \tag{2.1}$$

Parameter	Ocean	Ice	Salt
T [°C]	15	-51	30
$\langle v \rangle$ [m/s]	1530	3920	4560
β [K^{-1}]	25.5×10^{-5}	12.5×10^{-5}	11.6×10^{-5}
C_p [J/kg/K]	3900	1720	839
peak freq [kHz]	7.7	20	42
Gruneisen constant: $\gamma = \langle v \rangle^2 \beta / C_p$	0.153	1.12	2.87
maximum practical volume	10^5 km$^2\times$3 km	10^4 km$^2\times$1 km	$3\times4\times5$ km^3

Table 2.1: Acoustic coupling parameters taken from [36]. The neutrino-induced pressure signal scales with the Gruneisen constant.

For sea water, the parameters are $c = 1500$ m/s for the speed of sound, $\beta = 0.15\times10^{-3}$ K^{-1} for the coefficient of thermal expansion, $C_p = 3.8 \times 10^3$ Jkg^{-1}K^{-1} for the specific heat at constant pressure, and $\omega_0 = 2.5 \times 10^{10}$s^{-1} for the characteristic attenuation frequency. The characteristic attenuation frequency is strictly speaking a function of frequency as described in [53]. However, to simplify this calculation, a constant ω_0 is assumed in the frequency range of interest . The energy deposition is instantaneous, and thus is replaced by $E(\vec{r'}, t) = E(\vec{r'})\delta(t)$. The pressure wave in the far field can then be calculated using

$$p(\vec{r}, t) = \int E(\vec{r'}) G(\vec{r} - \vec{r'}, t) d^3\vec{r'} \tag{2.2}$$

where $G(\vec{r}, t)$ is the pressure pulse generated by a point source. Taking attenuation into account, $G(\vec{r}, t)$ has the form,

$$G(\vec{r}, t) = -\frac{\beta}{r\pi C_p} \frac{(t - r/c)}{r\sqrt{2\pi}\tau^3} exp(-(t - r/c)^2/(2\tau^2)) \tag{2.3}$$

where $\tau = \sqrt{r/(\omega_0 c)}$.

2.2.2 Shower Profile

The energy deposition profile, $E(\vec{r})$, is provided by the shower profile. While muon and tau neutrinos generate only hadronic showers, electron neutrinos also generate

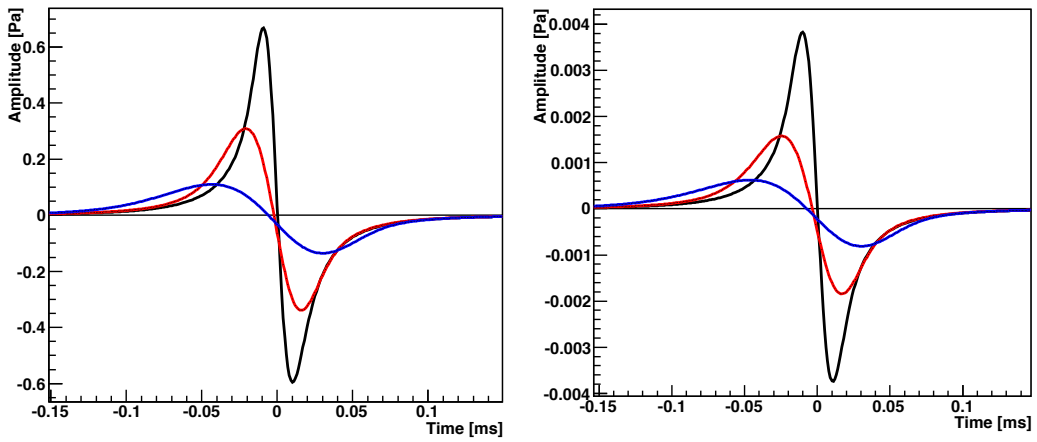

Figure 2.2: Simulated acoustic signals from a hadron shower of energy 10^{22} eV (left) observed at $r = 5$ km and 10^{20} eV (right) observed at $r = 8$ km at angles θ=0° (black), θ=0.5° (blue), and θ=1° (red).

electromagnetic showers superposed on hadronic ones. Because the electromagnetic shower is dominated by the Landau Pomeranchuk Migdal (LPM) effect [38, 39, 40, 41], the shower becomes elongated (∼300 m long) with large fluctuations in energy depositions and a weaker acoustic signal with irregular geometries. Therefore, we only consider hadronic showers, which exhibit a more consistent structure and a more predictable signal. The hadronic shower parametrization from [42] is used for $E(\vec{r})$. Hadronic showers of energy 10^{18}–10^{25} eV are 12–20 m long with the maximum energy deposition occurring at 6–14 m. Radially, most of the energy is deposited within 0.5 m of the shower axis. The fraction of neutrino energy deposited into the hadron shower, y, which is also known as the elasticity of scatter, is predicted to be on average $\langle y \rangle = 0.2$ for all flavors of neutrinos [43].

2.2.3 Signal Waveform

Fig. 2.3 shows signal waveforms p(t) calculated for different positions with respect to the shower. Because energy is deposited over a finite length, the acoustic signal has maximum pressure at observation angles nearly perpendicular to the shower axis. The observation angle θ is defined in the forward direction of the shower from the

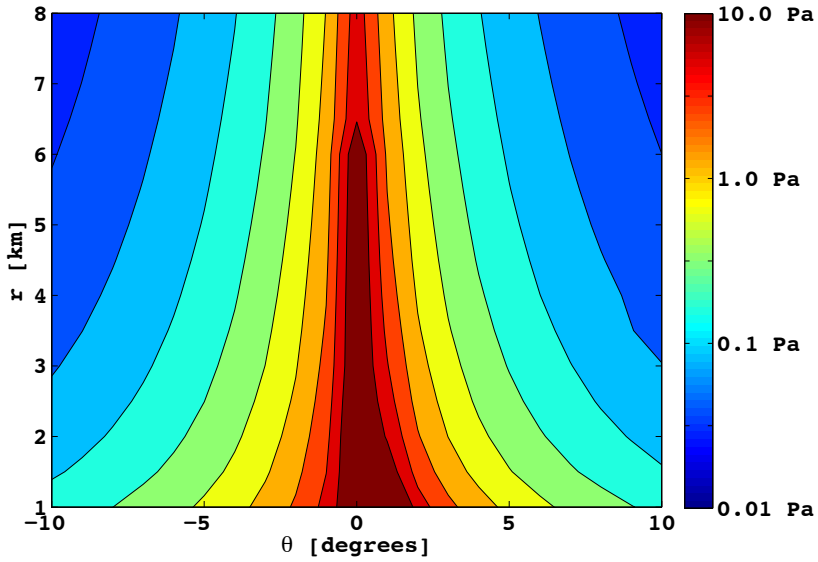

Figure 2.3: Pressure amplitude contours at varying observation points are shown for a 2×10^{23} eV hadronic shower.

perpendicular plane of the shower axis. The origin is at the starting point of the shower. The distance r is defined as the distance from the origin to the point of observation. Fig. 2.3 shows contours of the maximum pressure observed at varying θ and r for a 2×10^{23} eV hadronic shower.

2.3 Speed of Sound and Radiation Pattern

The speed of sound in the ocean varies with depth as shown in Fig. 2.4. This is due to the competing effects of temperature and pressure; an increase in either will correspond to a higher speed of sound. The profile of the speed of sound with depth varies at different locations of the ocean and also with the season. In the profile shown in Fig. 2.4, the ocean water is warmer towards the surface and pressure is higher towards the ocean floor, creating a sound channel with minimum sound speed at $\sim$1 km depth. The effect of this is the refraction of sound rays, much like an optical wave guide refracting light rays. This effect is illustrated in Fig. 2.4. For neutrino signals, the effect of the varying speed of sound amounts to the distortion

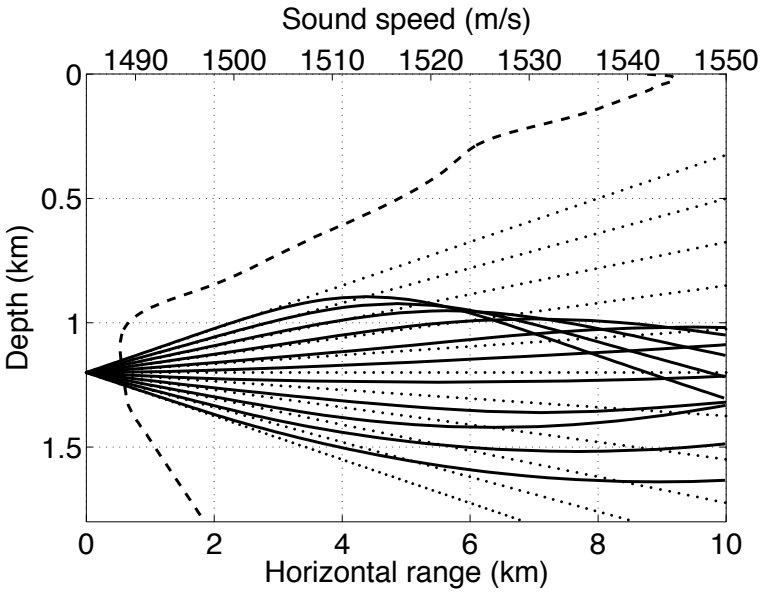

Figure 2.4: The speed of sound as a function of depth measured at the Tongue of The Ocean in the Bahamas averaged over all seasons. Using this, eleven rays are emitted from a point source at 1200m depth, from 5° below to 5° above the horizontal. Solid lines show the refracted rays due to the varying speed of sound. Dotted lines show unrefracted rays.

of the radiation pattern shown in Fig. 2.3 that is dependent on both the depth and direction of the shower.

Chapter 3

SAUND II Detector and Data

3.1 Detector

The second phase of SAUND (SAUND II) employs a large hydrophone array at the US Navy's Atlantic Undersea Test and Evaluation Center (AUTEC) located at the Tongue of the Ocean (TOTO) in the Bahamas. SAUND II is currently the largest test for the feasibility of acoustic ultra-high-energy neutrino detection. This program follows a general study of the expected performance [18], and a first experimental phase (SAUND I) using seven hydrophones [44]. Since then, the US Navy has upgraded the hydrophones and the readout system of the array. SAUND II uses 49 of these hydrophones with digitized signals transmitted to shore over optical fibers. The array spans an area of $\sim$ 20 km $\times$ 50 km with spacing of 3 – 5 km. Hydrophones are mounted 5.2 m above the ocean floor, at depths between 1340 m and 1880 m. Fig. 3.1 shows the configuration and the topography of the ocean floor. Hydrophones are omnidirectional with a flat response (within 5 dB) at the frequencies considered. The gains of the 49 channels coincide to within 1 dB. Analog signals are regenerated at the shore station from the digital data (by the US Navy for their backwards compatibility) and fed to the SAUND II data acquisition (DAQ) system that re-digitizes them at 156 kHz. Since low frequencies are not relevant for SAUND II, a hardware high-pass RC filter is applied to the analog data with a 3 dB point at 100 Hz.

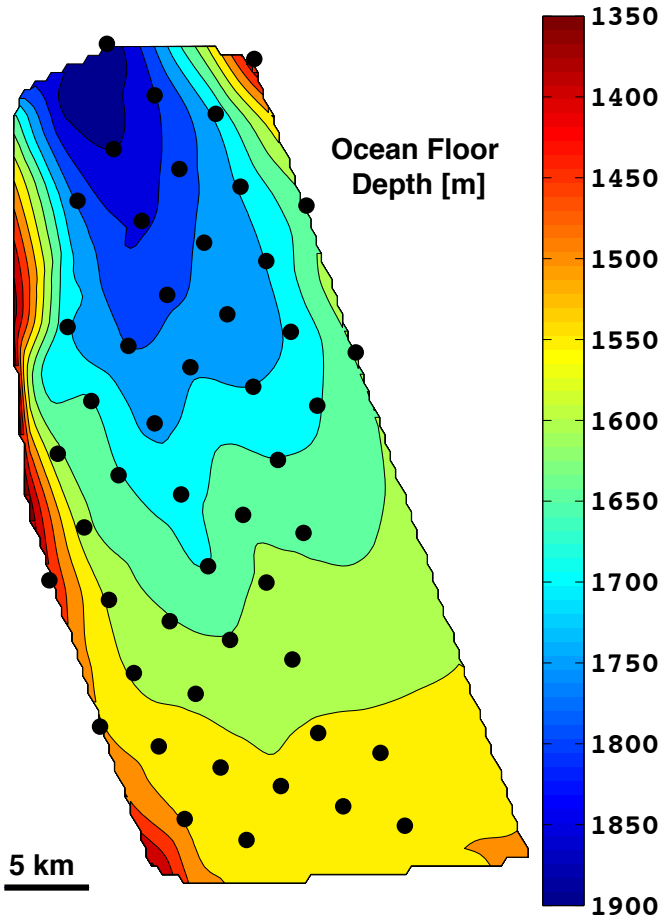

Figure 3.1: Layout of the SAUND II array. Hydrophone locations are marked by bullets. Color shows the depth of the ocean floor.

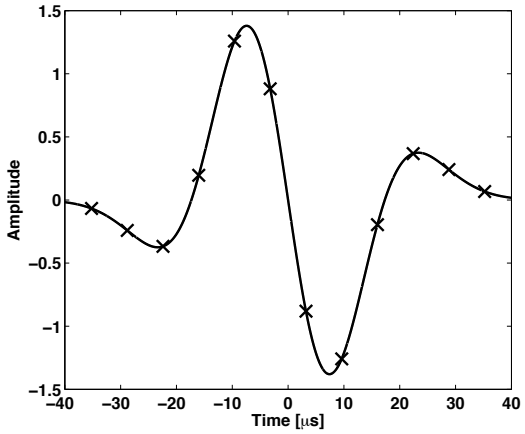

Figure 3.2: Bipolar response function used for online triggering. Markers show the digitized points used to match filter against the 156 kHz data sampling.

3.2 Data Collection

A DAQ program with real-time analysis running on seven PCs records candidate neutrino events using a matched filter with the bipolar response function shown in Fig. 3.2. Because the phase response of the electronic system is unknown, SAUND II only considers the absolute value of the matched filter. Once per minute, the trigger threshold on each hydrophone is adjusted independently to a value that would have acquired 20 triggers/min in the previous minute. Each hydrophone triggers independently, and a 1 ms time series of only the triggered hydrophone is recorded. In addition, every minute the threshold on each hydrophone is recorded. The noise conditions in the form of a power spectral density (PSD) and root mean square (RMS) are recorded every 5 s and 0.1 s respectively for each hydrophone.

The SAUND II DAQ system consists of seven National Instruments cards (NI-PCI-MIO-64)and eight PCs of which seven are dedicated to data acquisition and one for controlling the entire system. It also includes a front-end module with hardware high-pass filters and an IRIG timing signal distributor that connects to each of the cards. The NI ADC cards are controlled by COMEDI [45], and the DAQ software uses KiNOKO [46] as shown in Fig. 3.3.

During 2005 the DAQ system was installed and tested. One of the tests performed

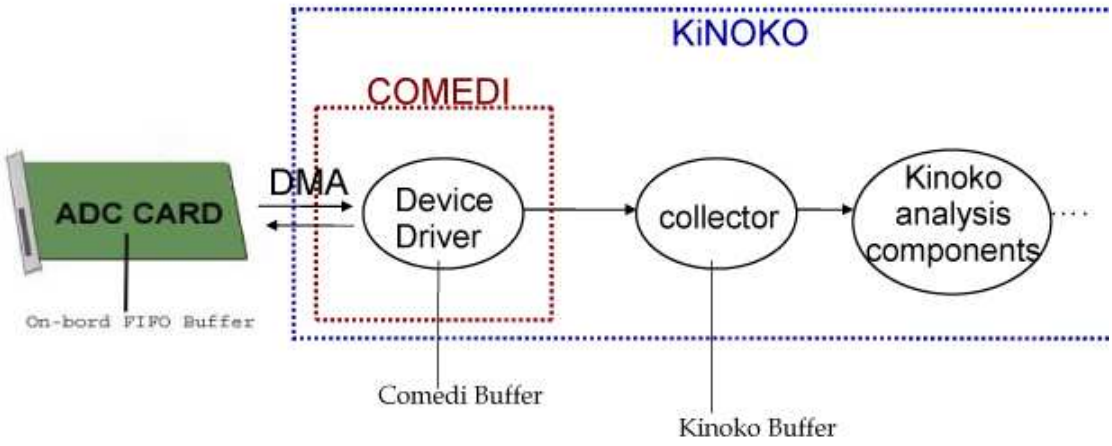

Figure 3.3: Schematics of data acquisition.

was the triangulations of light bulb implosions. Household A-19 light bulbs were tied to weights and dropped from a vessel on the surface at TOTO. Implosions of bulbs under high pressure of the deep ocean was heard by the SAUND II system. Triangulation of the implosion location was performed using only the acoustic information recorded by the SAUND II system. A comparison of the triangulated locations and the recorded bulb drop locations by GPS aboard the vessel is plotted in Fig. 3.4. The good agreement serves as confirmation that the system is installed and working properly, and triangulation of events can be performed.

From July 2006 to September 2007, the system ran under stable conditions. By agreement with the US Navy, the SAUND II data acquisition system records data only when the array is not otherwise in use. The system recorded a total integrated time of over 130 days.

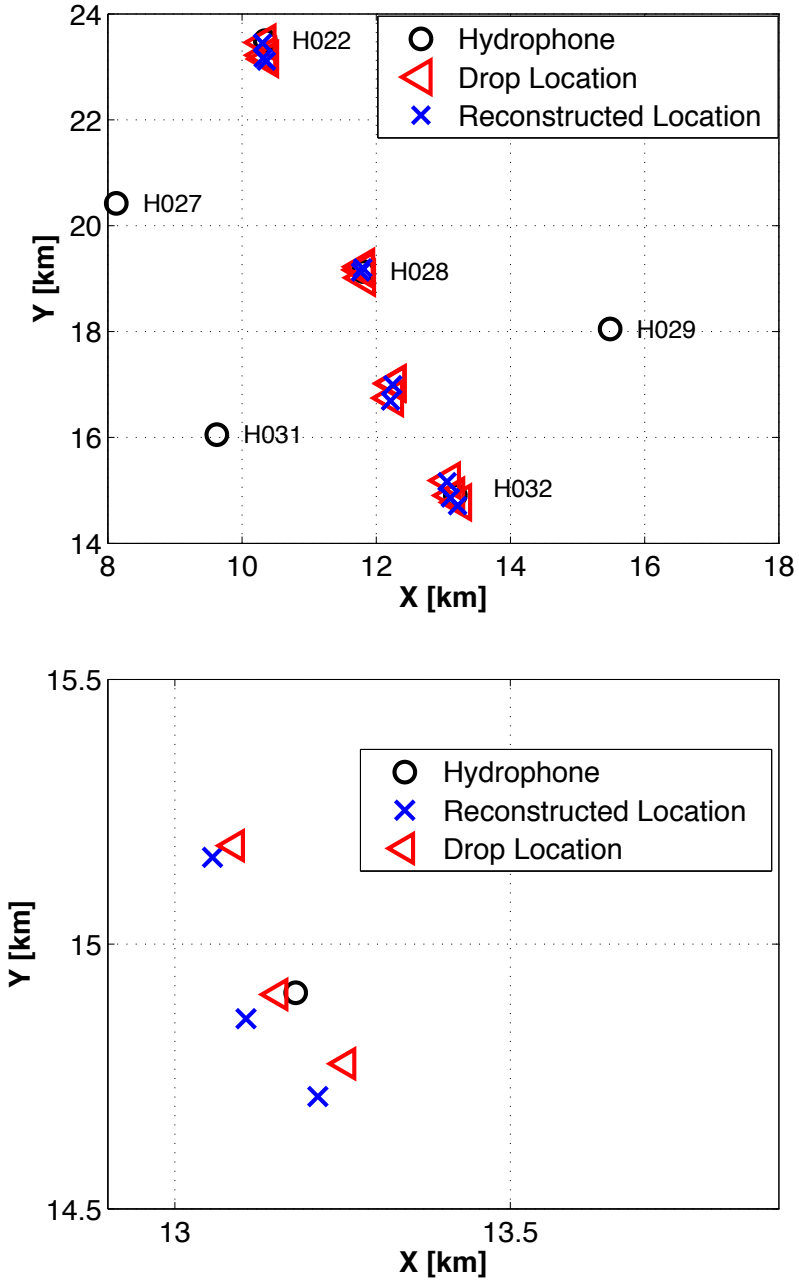

Figure 3.4: A comparison of the triangulated locations of light bulbs imploding and the recorded drop locations. A good agreement is observed confirming a successful DAQ system installation and triangulation. Bottom panel shows details of one of the clusters. Dominant cause of the difference is thought to be ocean tides sweeping the bulbs as it sinks.

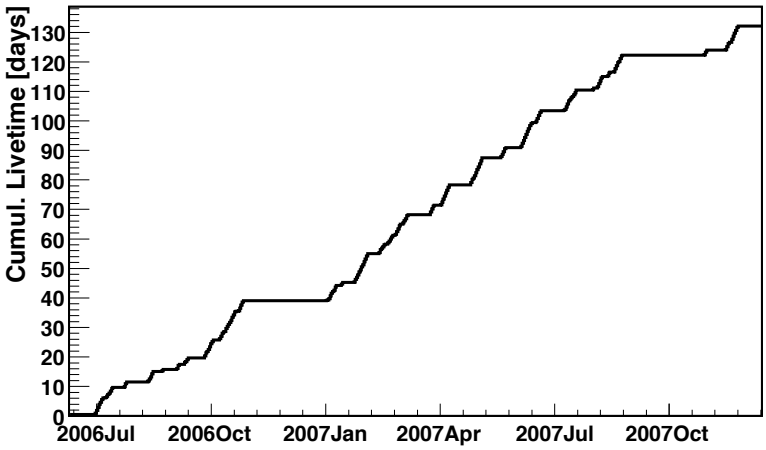

Figure 3.5: Accumulated livetime of the SAUND II experiment.

Chapter 4

Ocean Acoustics and Backgrounds

4.1 Introduction to Underwater Noise

The Bahamian ocean has many natural sources of background noise at the frequencies of interest. They can be loosely categorized into two types; transient noise and ambient noise. Transient background noise is mostly caused by marine life in the water and is characterized by short bursts of specific waveforms. Other transient noise can be caused by human activity such as ship traffic in the immediate vicinity. Transient backgrounds usually have characteristic time durations. Very rarely, high-amplitude noise causing significant disturbances throughout the array may disable the experiment for its duration. More frequently, transient noise caused by biological sources affect neutrino detection by causing false triggers. Ambient noise, on the other hand, is considered as the "permanent" broad spectrum background noise in the water. Usually caused by weather at the surface for frequencies of our interest, it is not expected to vary in short time durations or narrow frequency bands. "Sea state" is an oceanographic term used to describe the condition of the ocean surface, specifically the waves and swells. It is the primary indicator for the ambient noise profile to be expected undersea. Ambient noise can be thought of as the "noise" in "signal-to-noise," and affects neutrino detection by raising the lowest amplitude of the neutrino signal that is detectable.

Figure 4.1: Sperm whales, of which the most famous is Moby Dick [47], and snapping shrimp are two sources of background noise in the Bahamian ocean. Pictures from the Bahamas Marine Mammal Research Organisation, and Everest, Young, and Johnson [48].

4.2 Transient noise

Many biological species that vocalize at our frequencies of interest are known to exist in the Bahamian ocean. Sounds from mammals including a variety of whales and dolphins, crustacea such as the snapping shrimp (Fig. 4.1), and schools of fish may trigger as false neutrino signals or cause thresholds to move up. SAUND does not attempt to categorize recorded waveforms to these sources. However, some characteristics are easily identifiable as animal vocalization. The most easily recognizable waveforms in the SAUND II data set of triggered waveforms are the so called "diamond" events. They are few kHz to few tens of kHz with a diamond-shape envelope. Usually appearing in nearby hydrophones around the same time, they are seen in bursts for a duration of a few tens of seconds to a few minutes. Some have extremely high amplitudes (beyond the ± 3.15 Pa saturation of the SAUND II system), while others are below the ambient noise level and only detectable due to their high frequencies. The duration of the envelope can be anywhere from tens of μs to a ms.

Fig. 4.2 shows a range of diamond events.

4.2.1 Rate of Trigger

4.3 Ambient noise

Fig. 4.3 shows the expected ambient noise spectrum in the ocean. At frequencies below ∼10 Hz, seismic noise dominates and rolls off as a power law. Shipping noise is constantly heard in the range ∼20–50 kHz in most parts of the ocean, even if vessels are not seen in the vicinity. This is due to the long attenuation lengths at these frequencies and the heavy ship traffic around the world. Between 0.5 kHz and 50 kHz, the main source of noise is wind and waves at the surface of the ocean. Often called the Knudsen spectrum [50], it is expected to be a power law with overall levels that correlate to sea states. At high energies, thermal noise takes over as the dominant noise source.

4.3.1 Sea State and Ambient Noise Data

Ambient noise analysis are performed on a subset of SAUND II data, consisting of 11 data periods randomly selected between July to November 2006. Each data period consists of 24 hours of continuous data-taking by recording 6.56 ms integrated power spectral density (PSD) every 5 s on each hydrophone. In order to average out intermittent sources that are of transient nature, such as close-by ship traffic and fish feeding, all 17280 PSDs in a day are averaged to produce one spectrum for each hydrophone and every data period. For frequencies up to 15 kHz, the resulting 539 spectra all follow the expected $f^{-5/3}$ Knudsen shape. Therefore, the 1 kHz - 15 kHz region is used to unfold the sea state conditions. The ambient noise spectrum at sea state zero, in units of dB re μPa^2/Hz, is approximated from the average spectra presented in Urick [49] as

$$P(f) = 10\log(f^{-5/3}) + 94.5 \tag{4.1}$$

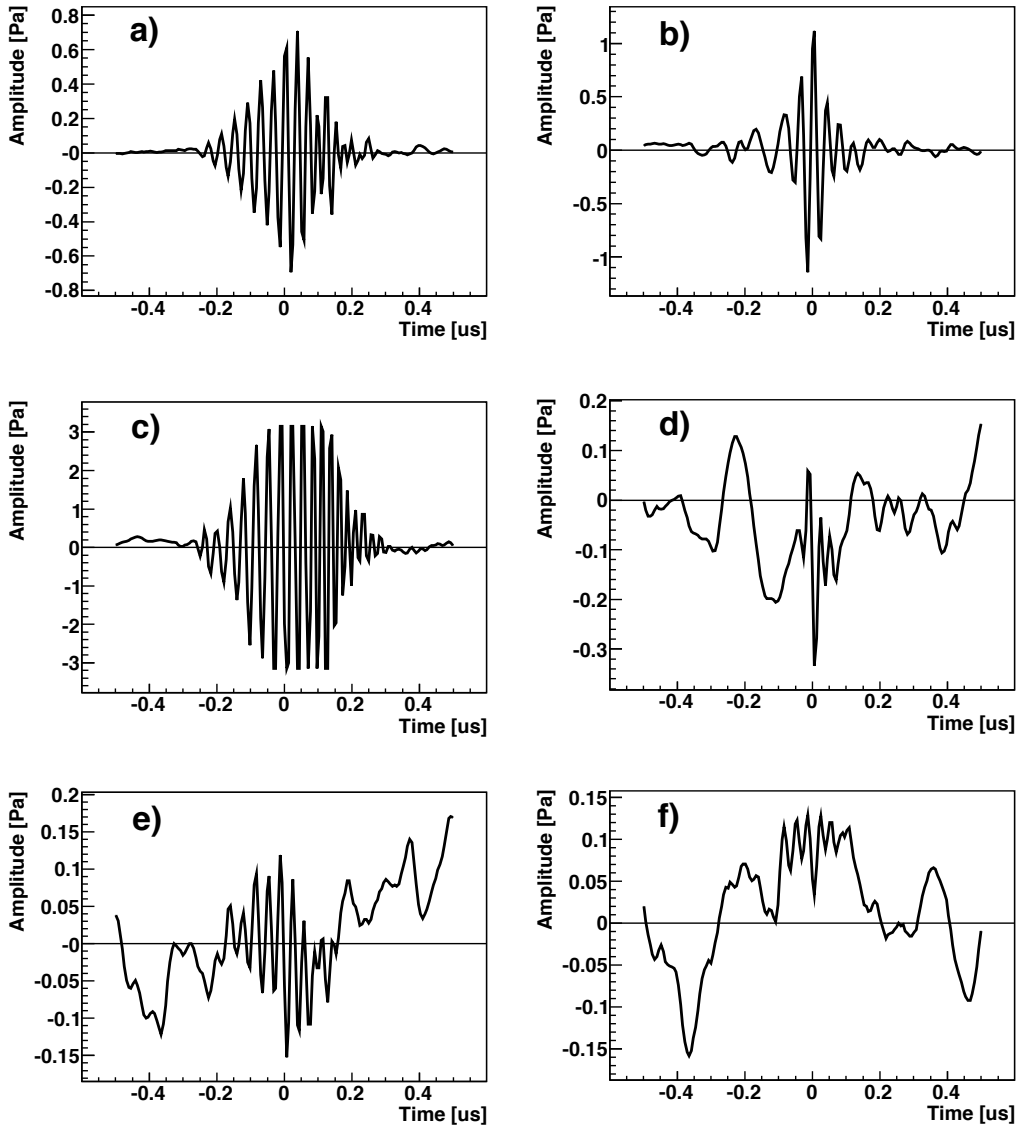

Figure 4.2: Various diamond events. Panels a) and b) are typical waveforms of different durations. Panel c) is is an extremely loud diamond event that saturates the ADC at ±3.15 Pa. Panels d), e), and f) are low amplitude diamond events of various types buried in noise.

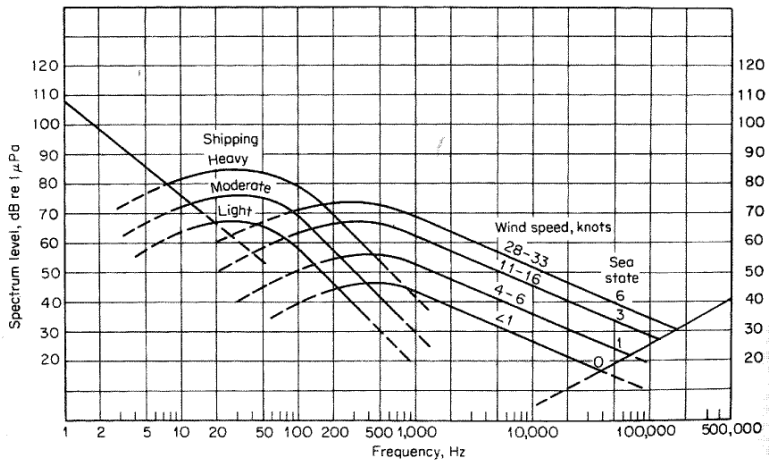

Figure 4.3: The well established model of the ambient noise spectrum of the ocean taken from [49]. Many fundamental studies of the ambient noise were conducted around World War II by the U. S. Navy, and were declassified later.

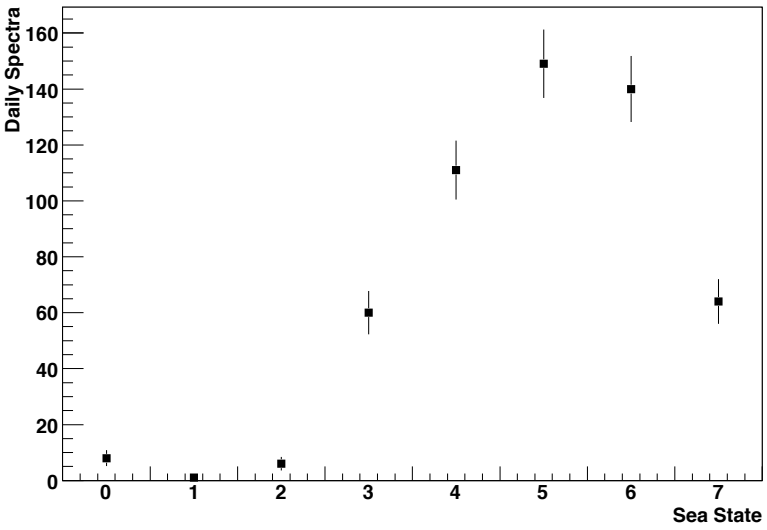

Figure 4.4: Histogram of daily averaged sea state calculated from 539 noise spectra taken by 49 hydrophones over 11 24-hour periods ranging from July to November 2006. The sea state 0 bin includes quiet periods calculated to be under the average sea state 0 noise level. Error bars indicate the magnitude of the statistical fluctuations.

for the spectral region of 1 kHz to 40 kHz. Since the dependence of the overall noise level on sea state does not influence the $f^{-5/3}$ falloff, noise levels for higher sea states can be found by adding to Eq. (4.1), $P_{ss} = 30\log(n_s + 1)$ where n_s represents the sea state [51]. The resulting analytical form becomes

$$P(f, n_s) = 10\log(f^{-5/3}) + 94.5 + P_{ss}(n_s) \tag{4.2}$$

with a continuous variable n_s in P_{ss} as the only free parameter to fit each PSD. Data are then fit to Eq. (4.2) using the least square method and equally weighing all frequencies from 1 kHz to 15 kHz. The discretized value n_s is used to produce Fig. 4.4. The fact that July to November encompasses hurricane season in the Caribbean, and hence volatile sea conditions, explains the relatively high daily averaged sea states measured.

After the fitted sea state quantity P_{ss} is subtracted from each spectrum, the resulting 539 full bandwidth ambient noise spectra exhibit remarkably similar shapes, even beyond the 1 kHz to 15 kHz range where the $f^{-5/3}$ power law no longer describes the slopes. Fig. 4.5a shows the spread in the data by plotting the envelopes containing 99% and 68% of the 539 spectra and their average after "sea state subtraction." It is apparent that while sea state conditions change drastically, the underlying ambient noise spectral shape, even at high frequencies, remains consistent. This is significant considering the different locations and seasons included in the analysis.

In order to check that the ambient noise spectra have shapes that are consistent over even shorter time scales, Fig. 4.5b plots the spread of the "sea state subtracted" spectra averaged over 5 min intervals measured on October 2nd 2006 at one hydrophone. Again the spread is presented in a manner similar to Fig. 4.5a, plotting the envelope containing 99% and 68% of the 287 spectra along with the average. The smooth features of the spectrum are stable. The extremely small spread in these spectra disfavors the possibility of intermittent sources contributing to daily averaged "sea state subtracted" spectra over the broad bands analyzed here. This suggests that if noise sources other than those causing surface noise give an important contribution, they must be continuous in time. Very few sources are identified as having a

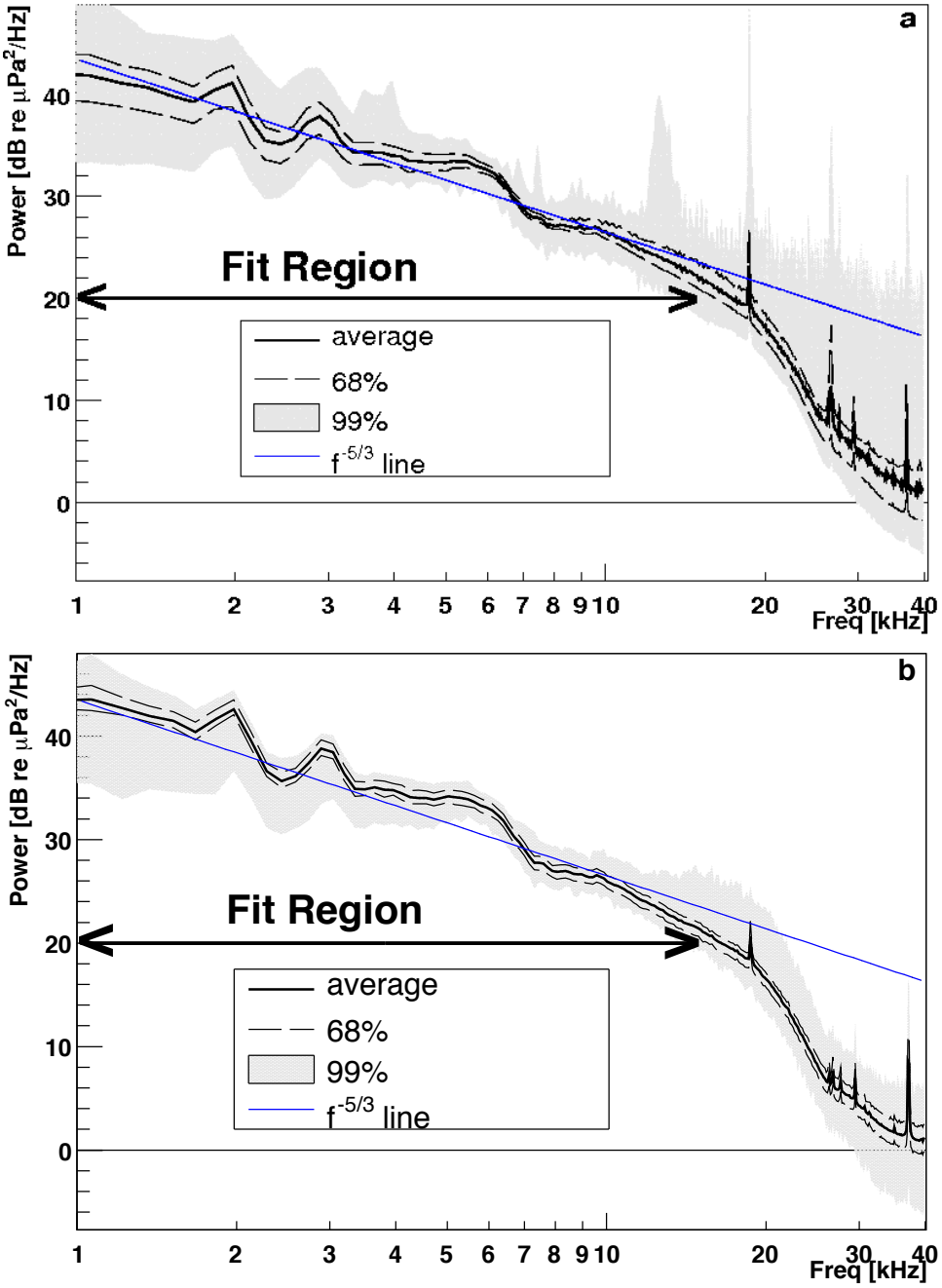

Figure 4.5: P_{ss}-subtracted power spectral density. The average of the daily (5 min) averaged spectra over 11 days (24 hours) and 49 (1) hydrophones is shown in a (b), along with the envelopes containing 99% and 68% of 539 (287) spectra.

steady all-day impact. Thermal noise is expected to become important at higher frequencies than measured here, while seismic background of continuous disturbance occurs far below 1 kHz [52]. Noise produced by marine biology is expected to have transient and narrow band characteristics. One well known exception is snapping shrimp beds, known for their consistent sound production underwater [48]. However, there is no evidence that shrimp beds exist at these depths, and the similarity of the spectra measured over an area of $\sim$1000 km^2 disfavors this possibility. Therefore, this analysis proceeds to directly test the hypothesis that surface generated noise is the only dominant broad band source contributing to ambient noise at these depths and frequencies.

4.3.2 Correlation with Wind

To verify that the overall noise level due to the sea state can indeed be expressed by Eq. 4.2, measured wind speeds are compared to the fitted value P_{ss} measured at the hydrophone closest to a shore anemometer station. Wind speeds, logged every 10 minutes at a site on Andros Island at a height of $\sim$15 m, 21 km away from the vertical of the hydrophone at a bearing of 110°, are shown in Fig. 4.6. In the Figure the direction of the wind and the quantity P_{ss} averaged every 10 min are also shown. The particular data period chosen for this study encompasses a rare occasion with a rather stable wind direction ($\simeq$ 100°) over a long period of time (12-hours). The Pearson product-moment correlation coefficient is computed between the first 300 min of P_{ss} data and an equivalent duration of wind data, applying different time offsets between the two. The correlation coefficient is shown as a function of the time offset in Fig. 4.7. The correlation coefficient reaches a maximum of 0.85 at a time offset of $\simeq$80 min. This is consistent with the delay expected from the distance, approximate wind speed and direction. In order to understand the statistical significance of this result, various 12-hour periods of wind data are randomly chosen from the 2006 year, and the same analysis is repeated using the original P_{ss} time series from Fig. 4.6. For each 12-hour period, a plot similar to Fig. 4.7 is produced, and the maximum correlation coefficient within the 0 to 420 min offset is chosen. Of 100 such 12-hour

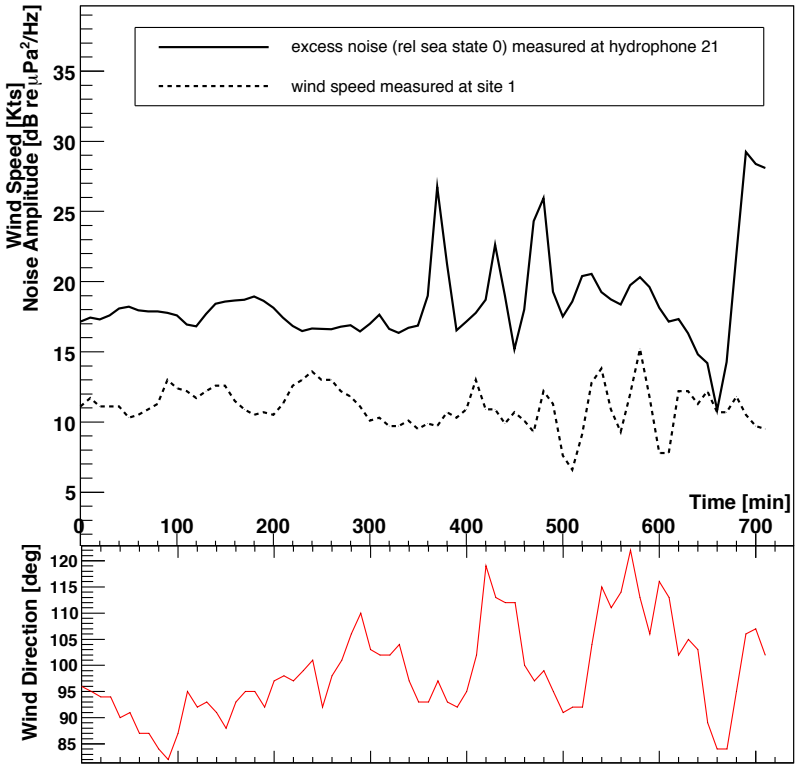

Figure 4.6: Wind speed and measured offset from the sea state zero, P_{ss}, as functions of time starting July 3rd 2006 at 0124 UTC (top panel). Wind direction is also plotted in degrees North (bottom panel). Wind measurements are taken at a site ∼21 km away in the range from the hydrophone used here.

wind data periods, only once a correlation coefficient higher than 0.85 was observed. Because the wind direction is usually quite variable over the travel time between the hydrophone location and the anemometer, conditions like those selected in Fig. 4.6 are rarely found. In addition there is no guarantee that the wind front stays coherent over the ∼1 hour travel to the anemometer station. Despite these limitations, however, it appears that a clear correlation is observed between the quantity P_{ss} and the wind strength.

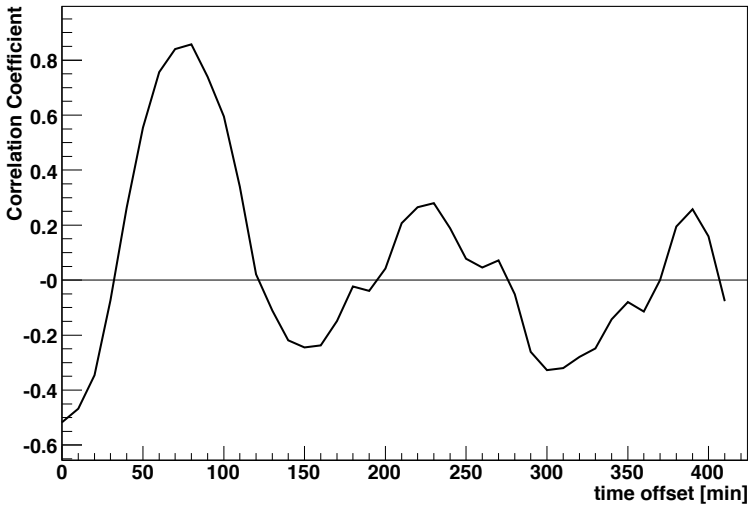

Figure 4.7: Correlation coefficient between the first 300 minutes of noise data from Fig. 4.6 and the equivalent period of wind speed data starting at different time offsets (horizontal axis). The main maximum at a time offset of $\sim$ 80 min is followed by substantially less significant maxima due to the spikes of the quasi-periodic wind at times between 500 and 600 min.

4.3.3 Depth Dependent Ambient Noise Spectrum

Shown in Fig. 4.8 is the average of 539 ambient noise spectra measured without subtracting the increased noise level at different sea states. The expected Knudsen form of Eq. (4.2) is also plotted with a P_{ss} value that fits the average best between 1 kHz and 15 kHz. This analytical spectrum reproduces the data well in this range. Above this frequency, however, it substantially overestimates the noise. Next, a depth-dependent modification developed by Short [51] is used to modify Eq. (4.2) to account for the large depth. Short's model considers the frequency dependent absorption that becomes significant when hydrophones are placed in deep waters, and thus, the distance from the surface where the noise originates becomes large. This modification is particularly important at high frequencies as absorption becomes substantial. The effective noise intensity per unit band received by an omnidirectional

hydrophone located at depth h, is given by

$$J_o(ah) = 2\pi J_\infty \int_0^{\pi/2} \cos^{n-1}\theta e^{-ah\sec\theta} \sin\theta d\theta \tag{4.3}$$

where J_∞ is the amplitude of the average intensity per unit band per unit solid angle radiated by a unit surface area, θ is the angle of the ray arriving at the hydrophone measured from the upward vertical direction, and $a = a(f)$ is related to the sound absorption coefficient $\alpha(f)$ by $\alpha h = -10\log(e^{-ah})$. The index n is 1 (2) for surface monopole (dipole) sources. Short calculates that the noise field below the horizontal plane of a hydrophone ($\theta > \pi/2$) at a height 91 m above the ocean bottom is significantly smaller than that above the horizontal and can be neglected. Therefore, Eq. 4.3 is integrated up to $\theta = \pi/2$ only taking into account direct paths from sources. Other assumptions made in deriving Eq. 4.3 are that the noise at the hydrophone is the incoherent sum of all intensities arriving, after attenuation, from the surface sources and that straight ray propagation is adequate [51]. Thus, the depth dependent correction to the Knudsen spectra can be determined by adding the following expression to Eq. (4.2).

$$10\log[J_o(ah)/J_o(0)] \tag{4.4}$$

In evaluating this frequency dependent offset, the average depth of the 49 hydrophones, $h = 1631$ m, is used. The sound absorption in sea water is parametrized according to Fisher and Simmons [53] to evaluate $\alpha(f)$ and therefore $a(f)$. A temperature profile taken at TOTO every 7.6 m down to 1830 m is used in this evaluation. The resulting offset is always negative, as expected for an attenuation, and is applied to Eq. (4.2). The result is also plotted in Fig. 4.8.

An attempt to further improve the theoretical curve is made by considering the frequency-dependent directionality of the hydrophones above 15 kHz. This is obtained by modifying Eq. 4.3 into

$$J_{eff}(ah) = 2\pi J_\infty \int_0^{\pi/2} \cos^{n-1}\theta e^{-ah\sec\theta} g(\theta, f) \sin\theta d\theta \tag{4.5}$$

with the response function $g(\theta, f)$ provided as a look-up table by the hydrophone specifications. Eq. 4.4 is then evaluated numerically and plotted in Fig. 4.8. It should be noted that the P_{ss} fit to the data in both of the modified Knudsen spectra is performed after the Eq. 4.4 correction and therefore, the numerical values of P_{ss} are slightly different in all 3 curves. Also noteworthy is the fact that although using $n = 1$ and $n = 2$ create very small differences as also shown by Short[51], the first case (monopole) produces a slightly better fit to data and is, therefore, used in the figure. However, the quality of data is not sufficient to significantly distinguish between the two models. Clearly the curves including attenuation provide better descriptions of the data at high frequency. Above 25 kHz the data appear to flatten faster than the model. It is unclear as to whether this should be considered a real underwater effect or simply due to difficulties in modeling the response of the hydrophones. It should be pointed out that the levels are too high to be considered as onset of thermal molecular noise, also shown in Fig. 4.8.

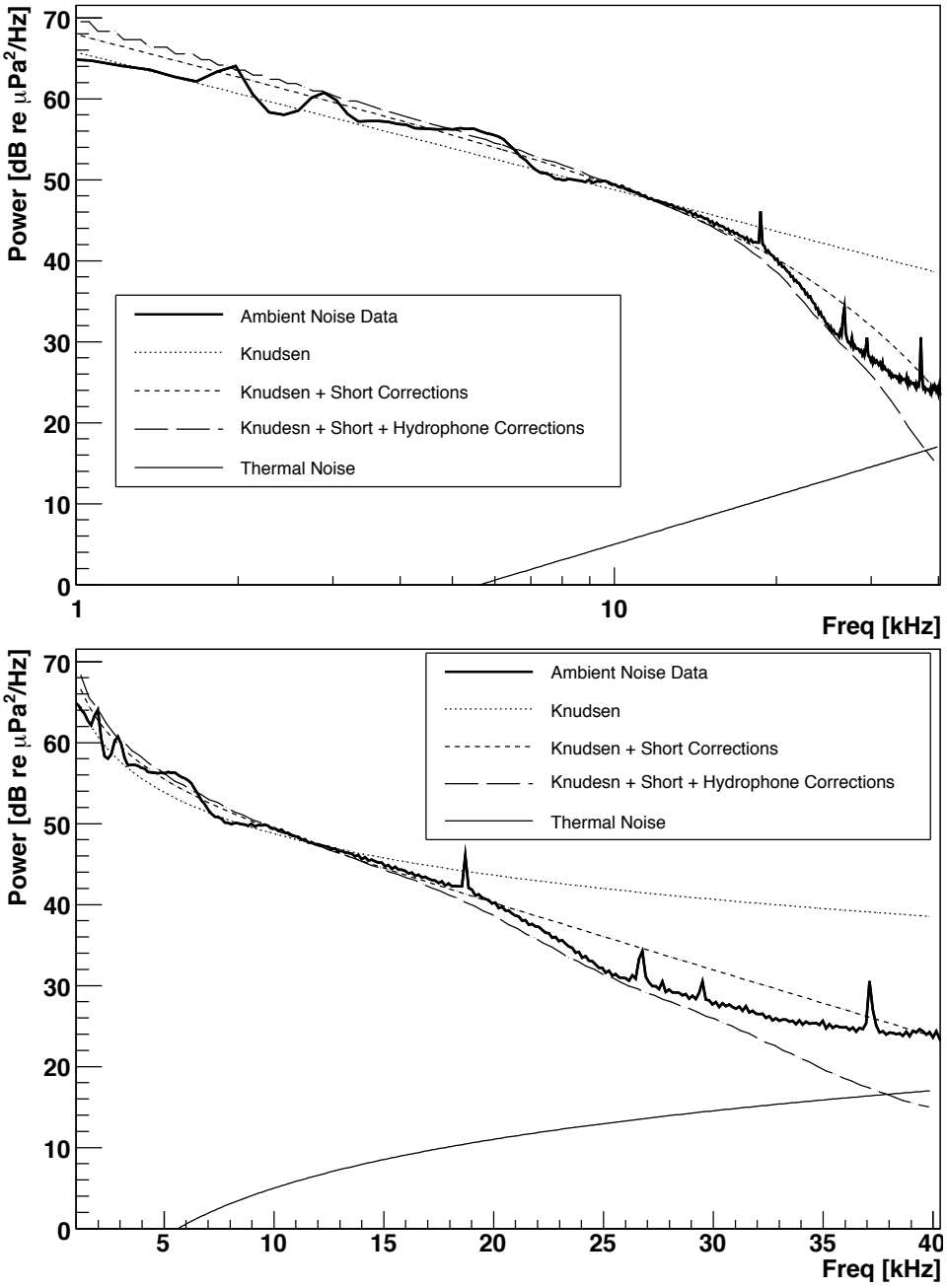

Figure 4.8: The average ambient noise measured, plotted in log (above) and linear (below) frequency scale with 3 theoretical curves of Knudsen spectra, as discussed in text. The theoretical curve for thermal noise[49] is also plotted. The curves labeled "Short corrections" in the legend include frequency dependent attenuation parametrized by Fisher and Simmons [53].

Chapter 5

Candidate Event Selection

Data analysis cuts are applied to the accumulated triggers in order to search for UHE neutrino signatures. Table 5.1 shows the total number of triggers accumulated and the size of the remaining data set after selection cuts are applied. In order to establish analysis cuts that are minimally biased, an 8% subset of trigger data was initially used to establish the data reduction cuts. Because the noise environment can vary greatly depending on time of day and season, the subset was selected carefully to have a random distribution in time. Once the full data was processed, it was found that some triggers are artificially generated by cross-talk between read-out channels. This effect was not discovered in the reduced data set as it affects a very small fraction of triggers. Cuts 1 through 3 result from analyzing the 8% data alone. Parameters for cuts 4 to 7 have been modified on the full data set to eliminate triggers caused by cross-talk while maintaining efficiency for neutrino showers. The method used to validate this procedure is described in Chapter 6.

Cuts 1 through 4 are applied on single-hydrophone triggers. After the source position in the ocean is triangulated using time difference of arrival, characteristics of these multi-hydrophone acoustic events are used on further cuts to test their consistency with expected properties of neutrino showers.

Cut	Single-phone Triggers	Events
1. Online Triggers	327.9M	—
2. Quality Triggers	146.7M	—
3. Waveform Selection	2,814,545	—
4. Single Phone Rate	2,562,047	—
5. Triangulation	6,605	4,995
6. Isolated Event	1,227	320
7. Radiation Pattern	8	2

Table 5.1: Data reduction process. The remaining number of single-hydrophone triggers after each cut is shown in the second column. The third column shows the number of acoustic events which are formed by four triggers that triangulate to a point in the ocean.

5.1 Analysis Cuts

In Table 5.1, the number of **Online Triggers** is the total number of triggers recorded by the online DAQ system in all hydrophones. Minutes of individual hydrophones with high threshold (>0.04), high trigger rate (>500 triggers/min compared to the target 20 triggers/min set by the DAQ), high trigger rate on a nearest neighbor, or man-made noise in the water are excluded to select **Quality Triggers**. Man-made noise can contaminate large parts of the array, and can be identified by narrow-band frequencies continuously dominating a wide area of hydrophones. This condition occurred a total integrated time of 9 min. Furthermore, data periods where the input cables appear to be disconnected are also removed. Such periods have unphysical, low noise levels, and are attributed to Navy personnel disconnecting individual cables for diagnosing problems in their system. One hydrophone had to be excluded entirely due to the majority of data belonging to this condition. For the remaining 48 hydrophones, this condition excludes ∼6% of integrated livetime.

Waveform Selection is used to further reduce background triggers. For each trigger, the online data acquisition system records a 1 ms waveform centered around the time of trigger. The absolute value of the matched-filter time series, $M(t)$, is calculated using the response function shown in Fig. 3.2 for each time series. The

Waveform Selection cut is based on two parameters from this time series: the peak area ratio (PAR) and the Gaussian width (GW). The PAR is obtained by dividing the value of M obtained at the time of trigger by the integral of M in the 1 ms window; PAR=$M(t_0)/\int_{t_0-0.5\ ms}^{t_0+0.5\ ms} M(t)dt$ where t_0 is the time of trigger. This quantity measures the significance of the trigger compared to its surrounding times. The GW is obtained by smoothing the time series of $M(t)$ to obtain the envelope shape, fitting this to a Gaussian, and extracting its width. For neutrino-induced signals, the width should be $\sim$40 μs. Many marine animals vocalize around frequencies of interest for this work. However, the signals originating from such sources tend to have a larger GW value. Fig. 5.1 compares these parameters for two triggers from the data set. The distribution of these parameters and the cut region where neutrino showers are expected are shown in Fig. 5.2. Triggers consisting of at least one data sample that saturate the ADC at $\pm$3.15 Pa bypass this cut and are kept regardless of the PAR and GW parameters.

The **Single Phone Rate** cut removes surviving triggers that occur on a single hydrophone clustered in time. Triggers accompanied by 10 or more triggers in any 5 s window are removed. In addition, triggers that occur less that 10 ms from each other are also removed. These rates are significantly higher than the 20 triggers/min target trigger rate set by the DAQ. Diffused, steady state UHE neutrinos are not expected to arrive and interact in bursts, so the removal of clustered triggers on single hydrophones only affects the livetime. Marine animals and artificial sources are usually responsible for such trigger patterns.

With the remaining triggers **Triangulation** is performed. The 6,605 triggers produce 4,995 source locations in the ocean by requiring four hydrophones to have the appropriate difference in arrival times. The time difference of arrival method used is described in [44] and includes the effects of the depth-dependent speed of sound in the ocean. Only hydrophones that are within 8 km of the hydrophone of earliest arrival time are considered for each event. For each event, a local rectangular coordinate system tangent to the Earth surface, centered around the earliest arrival-time hydrophone is used. High rates of trigger on a single hydrophone in the coincidence time window ($\sim$8 s) produce combinatorics such that a single trigger can be involved

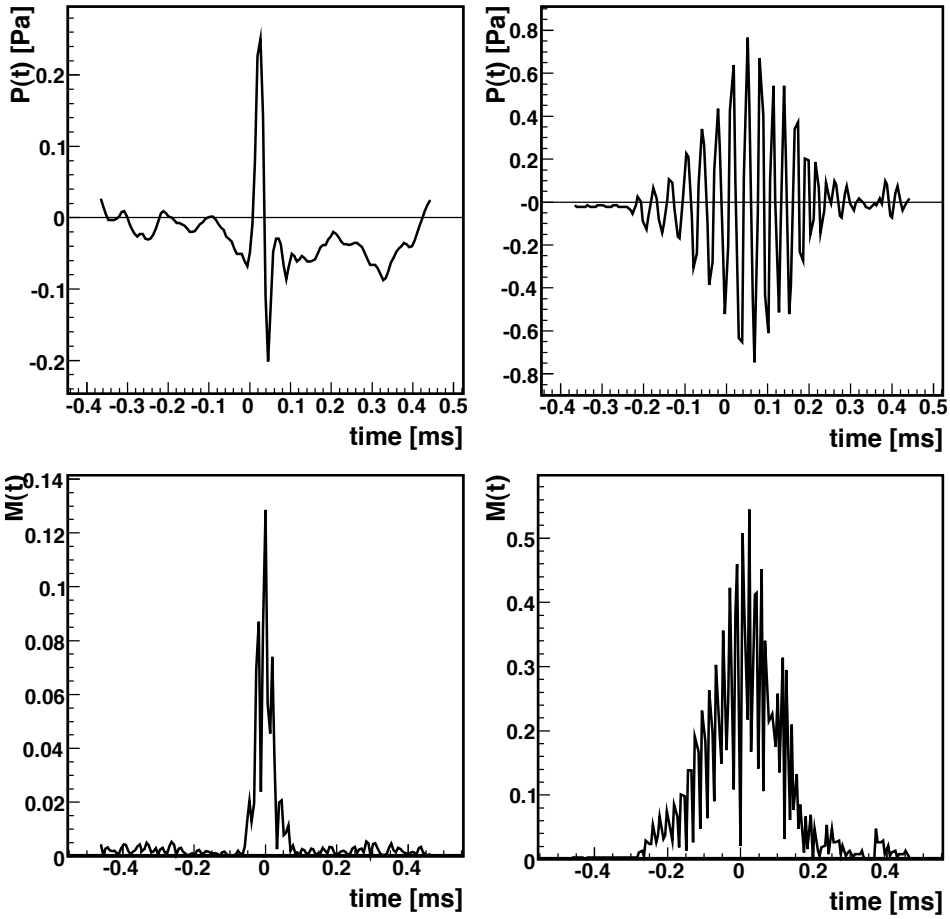

Figure 5.1: Examples of Waveform Selection. The top panels show the time series, P(t), around two different triggers from the SAUND II data set. The panels at the bottom represent their matched filter time series M(t) calculated with the $\sim$76 μs bipolar response function, shown in Fig. 3.2, in 6.41 μs time steps. The GW parameter is obtained by smoothing M(t) and fitting to a Gaussian. The trigger on the left yields PAR=0.13 and GW=36.6 μs. The trigger on the right yields PAR=0.02 and GW=97.9 μs. Even though the trigger on the right has a higher matched-filter value at the time of trigger, the PAR and GW parameters correctly discriminate between a trigger consistent with a shower (left) and a background event (right).

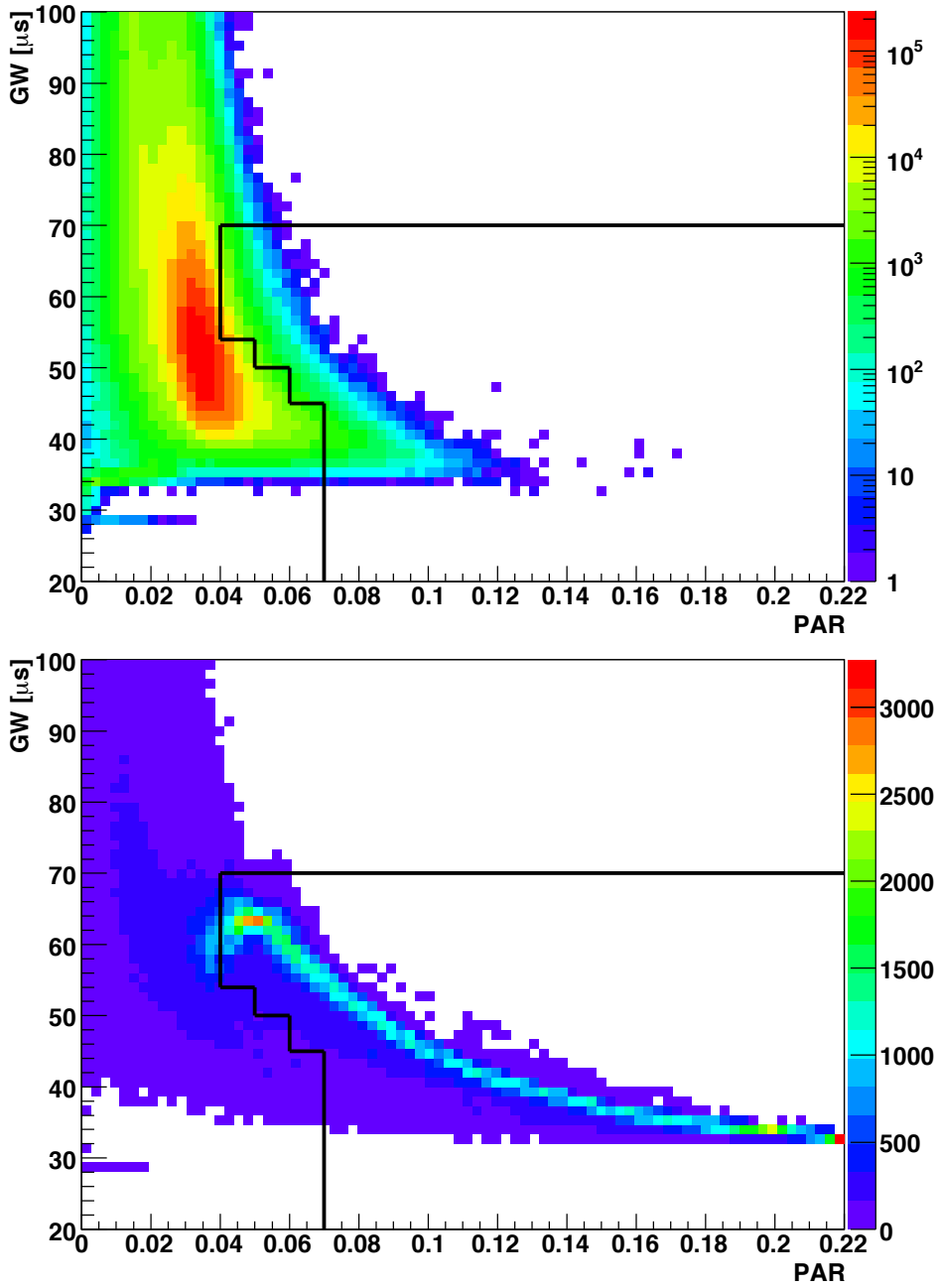

Figure 5.2: Distribution of the parameters and accepted region of the Waveform Selection (top panel). The peak corresponds to the Knudsen noise floor [54]. The 8% subset of data used to establish this cut is plotted. The accepted region was optimized by generating over 300,000 Monte Carlo signals from 10^{22}–10^{25} eV neutrino showers observed at angles -2°–2° at various distances and adding recorded noise (bottom panel).

in multiple events. However, by further excluding events that trigger the same hydrophone within a minute of each other, only 320 time **Isolated Event**s survive.

Since acoustic radiation from neutrino showers is not expected to be emitted spherically, but rather in a disk-like shape orthogonal to the direction of the shower [17, 18], only showers of certain energy and orientation combinations can produce pulses capable of triggering all four hydrophones from the triangulated event location. This geometric constraint utilizes the thresholds set at the time of the event, and only selects showers that are capable of triggering all four hydrophones with its acoustic radiation. However, not only does the radiation need to exceed the thresholds, but estimated pressure amplitudes must also be observed in the recorded waveforms. Only two events have observed pressures matching or exceeding those expected by geometrically possible showers, and pass the **Radiation Pattern** cut. A metric, $R_{missing}$, quantifies the ratio of pressure missing in the recorded peak pressure, P_{det}, from the estimated peak amplitudes, P_{est}.

$$R_{missing} = \frac{\sum_{i=1}^{4}(\Delta P)^2}{\sum_{i=1}^{4}(P_{est})^2} \tag{5.1}$$

where

$$\Delta P = \begin{cases} P_{est} - P_{det} & \text{for } P_{est} > P_{det} \\ 0 & \text{for } P_{est} < P_{det} \end{cases} \tag{5.2}$$

Since ΔP is defined as the pressure missing, it is set to zero for waveforms meeting or exceeding estimated pressure amplitudes. $R_{missing}$ is calculated for a dense grid of shower energy-orientation combinations for each event. Fig. 5.3 shows the minimum values obtained by considering all possible E_{sh}, θ, and ϕ configurations for each of the 320 events. 244 events did not have possible showers with any direction and energy less than $5{\times}10^{24}$ eV that fit the geometric constraint, and are assigned $R_{missing} = 1.0$. Events with $R_{missing} < 0.02$ pass the Radiation Pattern cut. The two events that pass require the shower energy to be 10^{24} eV$<E_{sh}<5{\times}10^{24}$ eV and 10^{22} eV$<E_{sh}<5{\times}10^{22}$ eV in order to be consistent with measured thresholds and peak pressures. These two events are discussed in detail in Chapter 7.

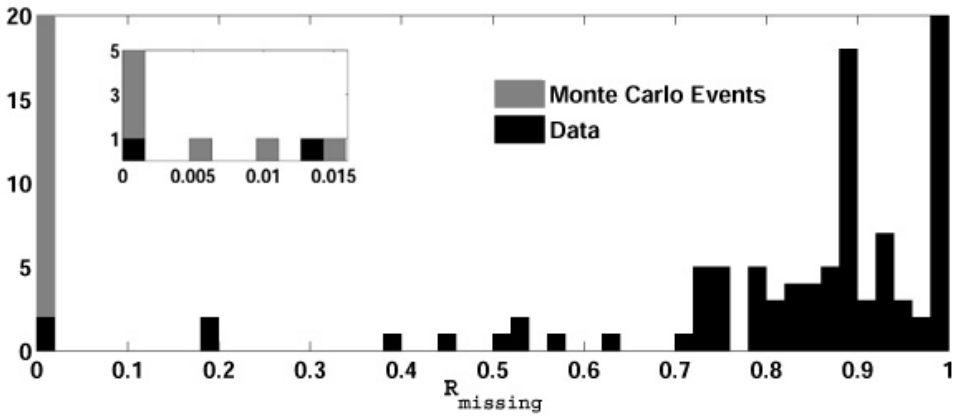

Figure 5.3: Error metric $R_{missing}$. The overflow bin at $R_{missing} = 1.0$ contains the 244 events with no possible shower geometries. The Monte Carlo events in the lowest bin extend beyond the maximum entries plotted to 131 events. The inset shows details of the distribution close to zero. Again, the number of Monte Carlo entries in the lowest bin extends to 128 entries.

Chapter 6

Efficiency and Sensitivity Estimates

The SAUND II detector is large enough to observe very different noise environments in different parts of the array. Therefore, the Quality Triggers cut described above removes livetime from single hydrophones minute-by-minute. Hence the configuration of enabled hydrophones is a complex pattern that varies from one minute to the next. To properly account for this, and to estimate the efficiency of the analysis cuts described above, neutrino events of different energies are generated by Monte Carlo simulation and injected randomly into the SAUND II livetime.

6.1 Generating MC Events

The Monte Carlo study uses ∼66M simulated neutrino events generated with the following distribution in zenith angle θ and depth z,

$$f_1(\theta, z) = Ae^{-z/lcos\theta}sin\theta \tag{6.1}$$

where l is the energy-dependent interaction length given by $l = 1/\sigma\rho N_A$. σ is assumed to scale with energy as $\sigma \sim (E_\nu[GeV])^{0.363}$ [35], ρ is the density of sea water, and N_A is the Avogadro constant. The events are generated uniformly in the azimuthal

angle ϕ as well as in latitude and longitude, in a 35 km×57 km rectangular area completely encompassing the SAUND II array. The closest hydrophone-boundary distance is >3 km. The fraction of neutrino energy deposited into the hadron shower, y, is generated with the distribution

$$f_2(y) = d\sigma/dy_{total} = d\sigma/dy_{cc} + d\sigma/dy_{nc} \tag{6.2}$$

where $d\sigma/dy_{cc} = (3 + 2(1-y)^2)y^{-0.67}$ and $d\sigma/dy_{nc} = (1 + (1-y)^2)y^{-0.67}$ [43]. The hadron shower energy is obtained by $E_{sh} = y \times E_\nu$. We assume the same distributions for all flavors of neutrinos. Ray tracing is performed between each hydrophone-event pair including the effects of sound speed variation in the ocean to obtain arrival times. The topography of the ocean floor is also considered. This produces some volume of ocean from where no rays can reach the hydrophones without intersecting with the ocean floor. An acoustic pulse is generated for each hydrophone-event pair using shower parameters [42] and attenuation. For each event, a time of occurrence is assigned with a distribution that is uniformly random in the SAUND II livetime. This allows the assignment of realistic noise conditions from the data to each hydrophone in each event.

6.2 Applying Cuts

Trigger candidates are then passed through the cuts in Table 5.1. First the matched filter values of the Monte Carlo candidate triggers are compared to the threshold set at the occurrence time and hydrophone. The Quality Triggers cut keeps only the triggers that were assigned a timestamp with good run conditions, while the Waveform Selection cut discriminates on simulated pulse shapes with added noise. The Single Phone Rate cut which is based on the rate of triggers on a single hydrophone can be affected by cross-talk. When a triggered waveform on one hydrophone produces cross-talk on other hydrophones that are also triggered, additional artificial triggers are created. The false increase in the trigger rate during this short period of time can affect the Single Phone Rate cut. To account for these situations, cross-talk triggers

are generated by using the arrival times of surviving triggers and creating additional triggers on hydrophones within 8 km (electronic cross-talk is instantaneous compared to both the speed of sound in water and the sampling frequency of the ADC cards). The Single Phone Rate cut and Triangulation are then performed including these false triggers. None of the artificial cross-talk triggers were found to generate events. The parameters used for the Single Phone Rate cut were chosen to minimize the rejection of true events in the presence of cross-talk.

The Isolated Event cut creates deadtime that is much less than 1% of the integrated livetime. Finally Radiation Pattern fitting is performed to confirm that the metric $R_{missing} < 0.02$, as shown in Fig. 5.3.

6.3 Effective Volume and Sensitivity

The efficiency of the SAUND II detector, $\eta = n_{detected}(E)/n_{generated}(E)$, is obtained at each decade of neutrino energy and shower energy. The effective volume, $V_{eff} = V_{gen} \times \eta$, where V_{gen} is the volume in which Monte Carlo events are generated, is shown in Fig. 6.1. Using the model-independent method described in [26], the sensitivity for UHE neutrino flux at different neutrino and hadron shower energies is plotted in Fig. 6.2 using a 90% confidence interval and assuming events remaining after cuts.

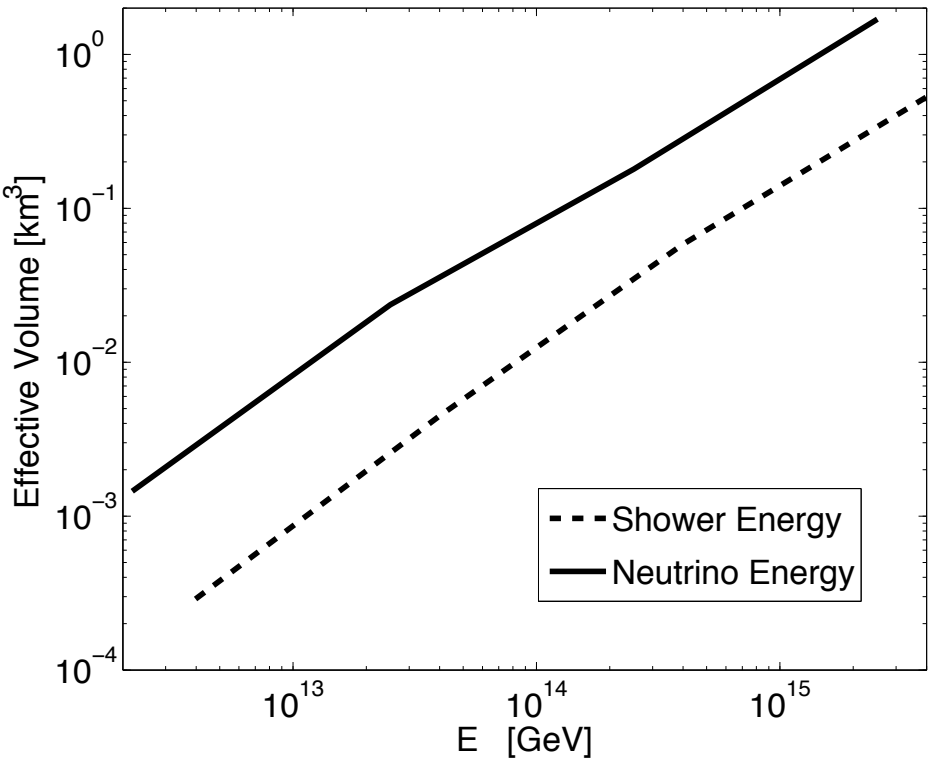

Figure 6.1: The effective volume of the SAUND II experiment for different neutrino and shower energies.

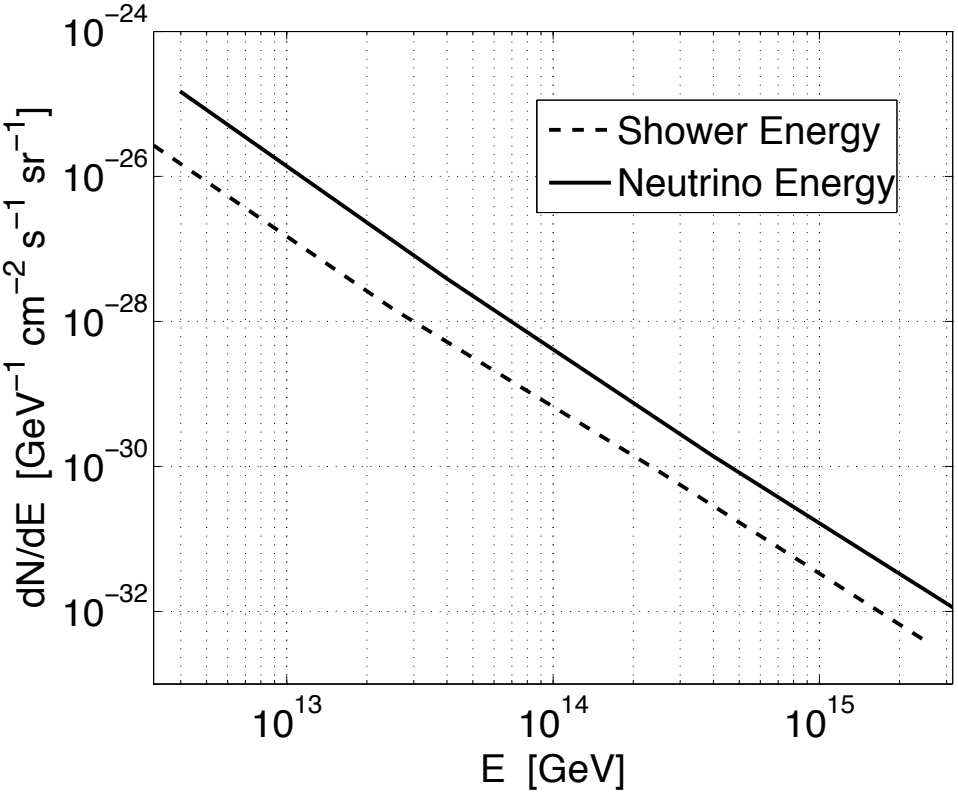

Figure 6.2: Sensitivity to UHE neutrino flux at 90% confidence level obtained by Monte Carlo study of the SAUND II experiment assuming no events are detected. The sensitivity is plotted for different neutrino and hadronic shower energies. Although on average neutrinos create hadronic showers that have ∼20% of its energy, the two plots are not simply a 20% shift from each other. This is due to the efficiency not scaling linearly with energy.

Chapter 7

Discussion and Results

7.1 Remaining Two Events

In order to formalize the SAUND II results, the two events surviving all cuts must be accounted for. The four triggers associated with each event are shown in Fig. 7.1 and Fig. 7.2. Further analysis capable of confirming the remaining two events as background or signal will require better understanding of the detector. Because the phase response of the system is unknown, the phase information of the triggered pulses is not utilized to discriminate events. Thus the event shown in Fig. 7.1 contains bipolar pulses with flipped phases, which are probably inconsistent as waveforms due to the same acoustic source. Apart from the phase, three of the four waveforms in Fig. 7.1 have similar high-amplitude bipolar pulses followed by a few more cycles of oscillation, while the fourth waveform on the top right has a much lower signal-to-noise. Since the probability of triangulating random arrival times to a single source location is extremely low, and since the four triggers are of order $\sim$100 ms to seconds apart, the origin of this event is assumed to be acoustic despite its peculiar features. Furthermore, the three high-amplitude waveforms are similar to a type of background repeatedly seen in the SAUND II data set. All but the waveforms in Fig. 7.1 are eliminated due to their high repetition rate during their occasional bursts. The triggers in Fig. 7.1, however, occur isolated in time and cannot be eliminated in such way.

As discussed in [55], the phase response of a hydrophone read-out system can

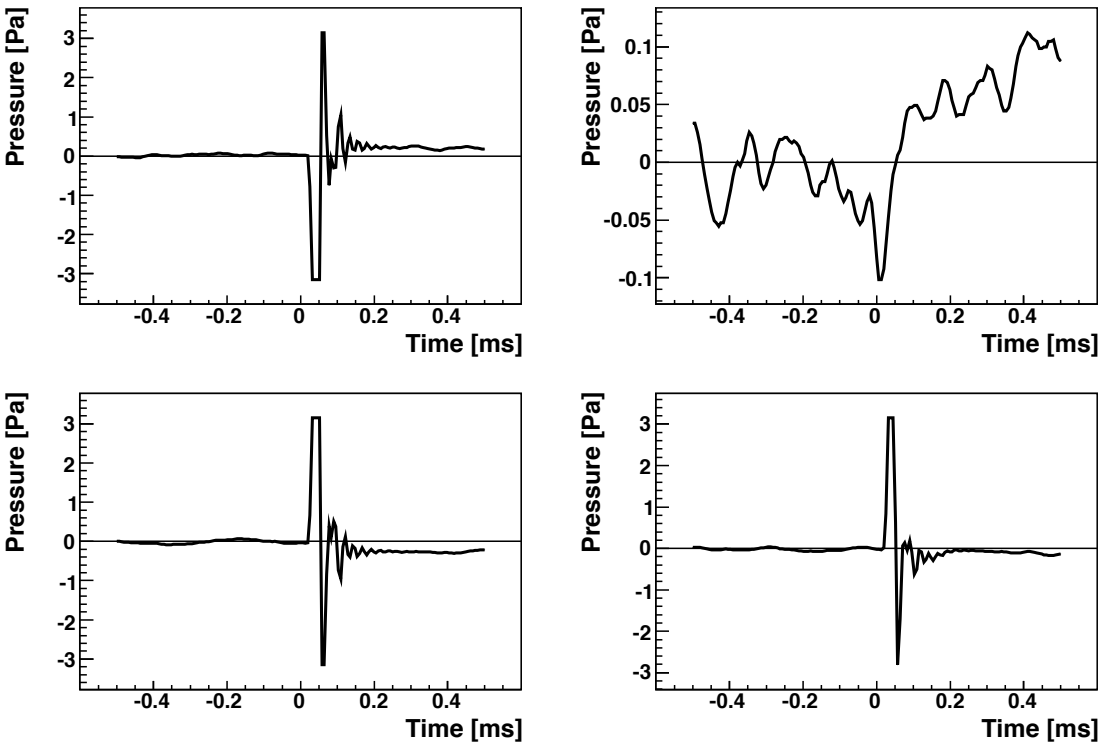

Figure 7.1: Waveforms of the four triggers associated with an event occurring 29 September 2006, 22:36:01.62 UTC compatible with shower energy 5×10^{24} eV$>E_{sh}>10^{24}$ eV, zenith angle $12.0°<\theta<16.0°$, and azimuth $170.7°<\phi<189.1°$ north. Three of the triggers saturate the ADC at ±3.15 Pa. Because the phase response of the electronic system is unknown, SAUND II only considers the absolute value of the matched filter, and the phase of the bipolar pulse is not used in this analysis.

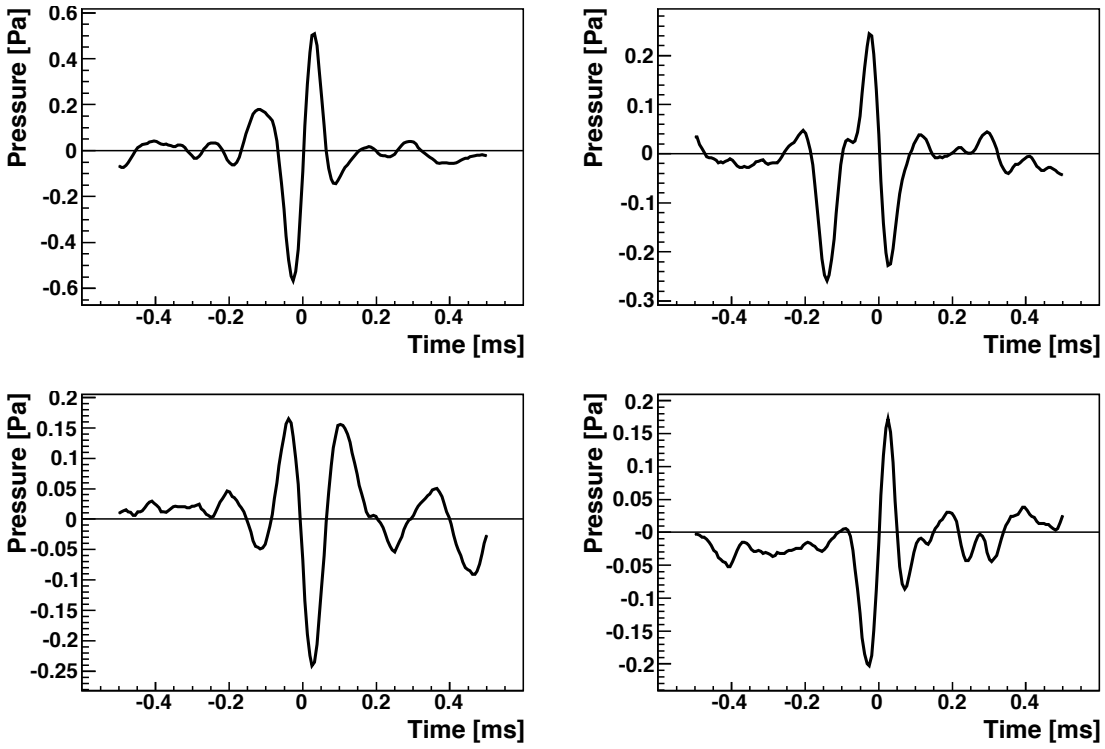

Figure 7.2: Waveforms of the four triggers associated with an event occurring 3 May 2007, 15:01:04.17 UTC compatible with shower energy 10^{22} eV$<E_{sh}<5\times10^{22}$ eV, zenith angle $6.3°<\theta<6.9°$, and azimuth $233.8°<\phi<235.5°$ north.

distort bipolar pulses into more cycles, creating multi-polar oscillation signals. For this reason, the Waveform Selection cut does not define or utilize the number of cycles of oscillation. Thus some of the waveforms shown in Fig. 7.2 are not clearly bipolar. In addition, because many triggers occur with amplitudes that are not significantly higher than the noise level, it is difficult to define how many peaks constitute a signal. This effect also compounds the difficulty in phase matching bipolar pulses.

7.2 Flux Upper Limit

Given the *a posteriori* observation made on two events, and the inability to perform a meaningful statistical analysis with such a small data set, an upper limit on the flux is set. Since the knowledge of impulsive backgrounds is incomplete, an upper limit with statistical significance on neutrino flux alone cannot be derived. Nevertheless, a conservative limit can be obtained by assuming that the two events are due to signal, and no other background is present. Following the treatment in [26],

$$s = \int \lambda(\varepsilon)\Phi(\varepsilon)d\varepsilon \tag{7.1}$$

where s is the expected number of events, λ is the sensitivity of the experiment at different energies, and Φ is the UHE neutrino flux. For a 90% confidence level,

$$\int \lambda(\varepsilon)\Phi(\varepsilon)d\varepsilon \leqslant s_{up} \tag{7.2}$$

where s_{up} is the 90% Poisson confidence interval upper limit of n event detection. At each neutrino energy bin, $s_{up}(E_{sh})$ is calculated for different shower energy ranges E_{sh}. For shower energy ranges 10^{24}–10^{25} eV and 10^{22}–10^{23} eV, $n = 1$ is used, making the upper bound $s_{up} = 3.9$. For other shower energy ranges, $n = 0$ is used, making the upper bound $s_{up} = 2.3$. At each neutrino energy, a weighted average $\langle s_{up} \rangle$ is calculated using

$$\langle s_{up}(E_\nu) \rangle = \sum_{E_{sh}} s_{up}(E_{sh}) \frac{N(E_{sh})}{N(E_\nu)} \tag{7.3}$$

where $N(E_{sh})$ is the number of neutrinos that will produce a shower in the energy range E_{sh} when $N(E_\nu)$ neutrinos are generated at neutrino-energy range E_ν. The weighted average gives $\langle s_{up}(E_\nu)\rangle$ at each neutrino energy, and is used to set a flux limit

$$\Phi(E_\nu) \lesssim \frac{\langle s_{up}(E_\nu)\rangle}{E_\nu \lambda(E_\nu)}. \tag{7.4}$$

The limit obtained by this method along with other experimental limits are plotted in Fig. 7.3. The SAUND limits are the only limits set by employing the acoustic technique. Other limits are set by searching for radio signals of UHE neutrinos.

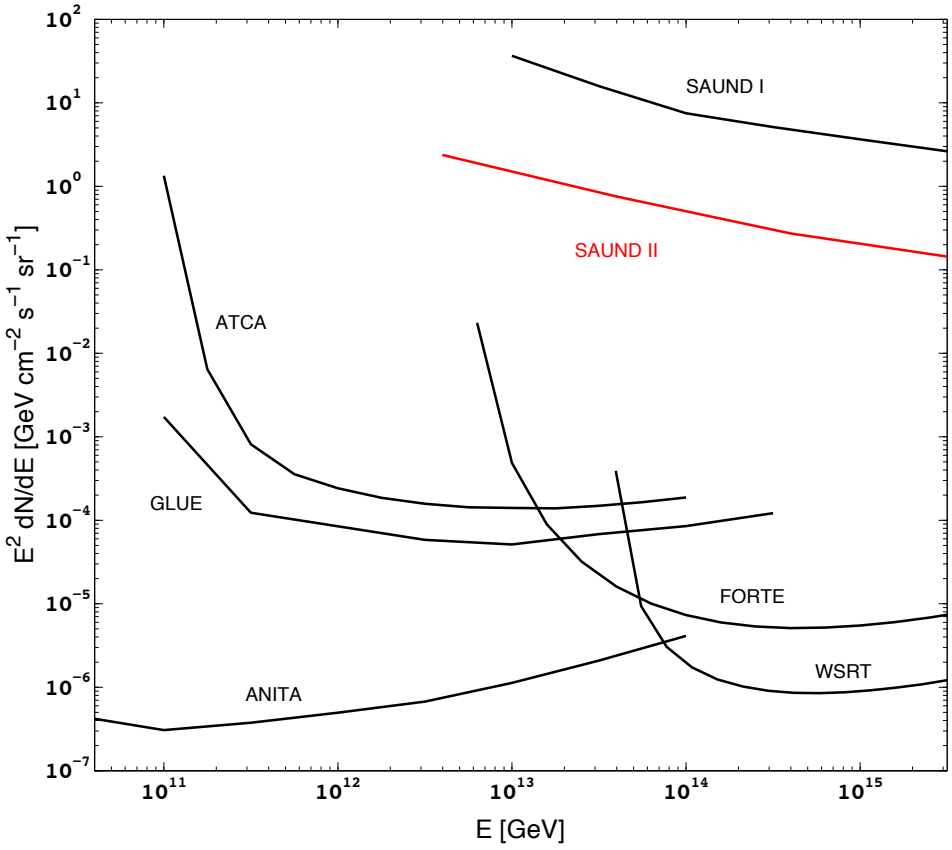

Figure 7.3: Neutrino flux upper limit from the SAUND II experiment. Various other limits are plotted: SAUND I [44], GLUE [29], FORTE [26], ANITA [28], ATCA-LUNASKA [30], and NuMoon-WSRT [31, 56].

Chapter 8

Conclusion

The SAUND II experiment demonstrates the feasibility of using a large-area acoustic-sensor array to detect UHE neutrinos. A full analysis capable of detecting very rare events consistent with shower-induced signals in a volatile noise environment with drastically different noise conditions in different parts of the large array has been developed and executed.

The analysis of a large acoustic noise data set collected at depths in excess of 1500 m and frequencies up to 40 kHz confirms that, even at substantial depths, a uniform surface distribution of sources alone is sufficient to describe ambient noise characteristics up to 25 kHz. A correlation observed between wind speed and overall noise levels at these depths during steady wind conditions further confirms this finding. A description of the spectral shape above 15 kHz is found to require, at the depths considered here, proper account of the sound attenuation in water. This depth effect must therefore be included when defining parameters in acoustic neutrino detection, such as the transfer function and the signal to noise ratio, that require the expected noise spectrum.

The sensitivity of SAUND II is limited by the larger hydrophone spacings and by hydrophones being mounted on the ocean floor. This results in a mostly flat and sparse two dimensional array which severely limits the sensitivity to the emission properties of showers.

Unambiguously identifying rare UHE neutrinos from either acoustic or radio signals in huge naturally occurring bodies subject to varying and poorly understood backgrounds is very difficult. Combining multiple techniques in a hybrid array featuring acoustic, radio, and/or optical detectors makes it possible to identify neutrinos by detecting two signals that have very different production and propagation mechanisms as well as backgrounds. In the absence of such an array, it is important to identify backgrounds. It was found that transient noise originating from discrete acoustic sources in the water causes the main backgrounds and limitation to the acoustic technique. A powerful cut, the Radiation Pattern cut, was developed to distinguish the geometry of emission to cope with such transient events. This cut will be significantly more effective when used with arrays of hydrophones arranged in all three dimensions. From such arrays, more information regarding the geometry of the emission lobe can be extracted.

Bibliography

[1] C. Dickens, *A Tale of Two Cities* (Chapman&Hall, 1859).

[2] J. Davis, Raymond, D. S. Harmer, and K. C. Hoffman, Phys. Rev. Lett **20**, 1205 (1968).

[3] K. S. Hirata *et al.*, Phys. Rev. Lett. **65**, 1297 (1990).

[4] R. Becker-Szendy *et al.*, Phys. Rev. D **46**, 3720 (1992).

[5] E. N. Alekseev, L. N. Alekseeva, V. I. Volchenko, and I. V. Krivosheina, JETP Lett. **45**, 589 (1987).

[6] C. Kraus *et al.*, Eur. Phys. J. C **40**, 447 (2005).

[7] Particle Data Group, Phys. Lett. B **667**, 1 (2008).

[8] A. Mantz, S. W. Allen, and D. Rapetti, MNRAS **406**, 1805 (2010).

[9] IceCube Collaboration, Astrophysical Journal **701**, L47 (2009).

[10] ANTARES Collaboration, Astropart. Phys. **31**, 277 (2009).

[11] P. Favali *et al.*, Nucl. Instrum. Meth **A**, In Press (2010).

[12] BAIKAL Collaboration, Astropart. Phys. **25**, 140 (2006).

[13] Pierre Auger Collaboration, Phys. Letters B **685**, 239 (2010).

[14] K. Greisen, Phys. Rev. Lett. **16**, 748 (1966).

[15] G. T. Zatsepin and V. A. Kuzmin, JETP Lett. **4**, 78 (1966).

[16] J. Cronin, T. K. Gaisser, and S. P. Swordy, Sci. Amer. **279**, 44 (1997).

[17] J. G. Learned, Phys. Rev. D **19**, 3293 (1979).

[18] N. G. Lehtinen, S. Adam, G. Gratta, T. K. Berger, and M. J. Buckingham, Astropart. Phys. **17**, 279 (2002).

[19] L. Sulak *et al.*, Nucl. Instrum. Methods **161**, 203 (1979).

[20] ACoRNE Collaboration, J. Phys.: Conf. Ser. **81**, 012011 (2007).

[21] IceCube Collaboration, Astropart. Phys. **33**, 277 (2010).

[22] NEMO Collaboration, (2008), astro-ph/0804.2913.

[23] ANTARES Collaboration, Nucl. Instrum. Meth. Suppl. A **604**, 158 (2009).

[24] BAIKAL Collaboration, (2009), astro-ph/0910.0678.

[25] ANITA Collaboration, Phys. Rev. Lett. **99**, 171101 (2007).

[26] N. G. Lehtinen, P. W. Gorham, A. R. Jacobson, and R. A. Roussel-Dupre, Phys. Rev. D **69**, 013008 (2004).

[27] I. Kravchenko *et al.*, Astropart. Phys. **20**, 195 (2003).

[28] P. W. Gorham *et al.*, Phys. Rev. D **82**, 022004 (2010).

[29] P. W. Gorham *et al.*, Phys. Rev. Lett **93**, 041101 (2004).

[30] C. W. James *et al.*, Phys. Rev. D **81**, 042003 (2010).

[31] O. Scholten *et al.*, Phys. Rev. Lett. **103**, 191301 (2009).

[32] G. S. Varner *et al.*, Nucl. Instrum. Meth. A **554**, 437 (2005).

[33] Pierre Auger Collaboration, Phys. Rev. D **79**, 102001 (2009).

[34] G. Barenboim, O. M. Requejo, and C. Quigg, Phys. Rev. D **71**, 083002 (2005).

[35] Gandhi *et al.*, Phys. Rev. D **39**, 093009 (1998).

[36] P. B. Price, J. Geophys. Res **111**, B02201 (2006).

[37] IceCube, (2010), arXiv:1004.1694.

[38] L. Landau and I. Pomeranchuk, Dokl. Akad. Nauk SSSR **92**, 735 (1952).

[39] L. Landau and I. Pomeranchuk, Dokl. Akad. Nauk SSSR **92**, 535 (1953).

[40] A. Migdal, Phys. Rev **103**, 1811 (1956).

[41] A. Migdal, Sov. Phys. JETP **5**, 527 (1957).

[42] J. Alvarez-Muniz and E. Zas, Phys. Lett. B **434**, 396 (1998).

[43] A. R. Beresnyak, (2004), arXiv:0310295.

[44] J. Vandenbroucke, G. Gratta, and N. Lehtinen, ApJ **621**, 301 (2004).

[45] Comedi - control and measurement device interface, `http://www.comedi.org`, Open soure drivers, tools, and libraries for data acquisition plug-in boards.

[46] Kinoko, `http://www.awa.tohoku.ac.jp/~sanshiro/kinoko-e/`, A general purpose online data acquisition system designed for high-energy physics experiments. Primarily developed for the KamLAND experiment.

[47] H. Melville, *Moby-Dick* (Richard Bentley, 1851).

[48] F. A. Everest, R. W. Young, and M. W. Johnson, J. Acoust. Soc. Am. **20**, 137 (1948).

[49] R. J. Urick, *Principles of Underwater Sound* (McGraw-Hill, 1983).

[50] V. O. Knudsen, R. S. Alford, and J. W. Emling, J. Mar. Res **3**, 410 (1948).

[51] J. Short, IEEE J. Ocean. Eng. **30**, 267 (2005).

[52] G. M. Wenz, J. Acoust. Soc. Am. **34**, 1936 (1962).

[53] F. H. Fisher and V. P. Simmons, J. Acoust. Soc. Am. **62**, 558 (1977).

[54] N. Kurahashi and G. Gratta, Phys. Rev. D **78**, 092001 (2008).

[55] S. Danaher *et al.*, J. Phys.: Conf. Ser. **81**, 012011 (2007).

[56] S. Buitink *et al.*, A&A (2010), arXiv:1004.027v1, preprint doi 10.1051/0004-6361/201014104.